Quartz-strain-rate-metry (QSR), an efficient tool to quantify strain localization in the continental crust.

E. Boutonnet[1,2] and P.H. Leloup[2]

1 Institute of Geosciences, Johannes Gutenberg University Mainz, J.-J.-Becher-Weg 21, D-55128 Mainz, Germany

2 LGL -TPE UMR CNRS 5276, UCB Lyon1 - ENS Lyon, 2 rue Raphael Dubois, 69622 Villeurbanne, France

Corresponding author: P. H. Leloup. LGL -TPE UMR CNRS 5276, UCB Lyon1 - ENS Lyon, 2 rue Raphael Dubois, 69622 Villeurbanne, France. herve.leloup@univ-lyon1.fr

Key points

- Local ductile strain rates can be measured at the quartz ribbon scale
- A special attention has to be paid to exhuming shear zones
- Strain localization is mapped by strain-rates variations across shear zones

Abstract.

Quantification of strain localization in the continental lithosphere is hindered by the lack of reliable deformation rate measurements in the deep crust. We describe the Quartz-strain-rate-metry (QSR) method, a convenient tool for performing such measurements at a cm-scale from the deformation of quartz, the most ubiquitous mineral in the continental crust.

We applied the QSR to two major continental strike-slip ductile shear zones, the Ailao Shan - Red River (ASRR, southwest China) and the Karakorum (KSZ, northwest India). The strain rates were determined by measuring the mean recrystallized quartz grain size, and the thermodynamic conditions of this recrystallization event. The deformation regimes were investigated using the Crystallographic Preferred Orientation of quartz. The pressure and temperature conditions were obtained combining the TitaniQ thermo-barometer and the local exhumation path of the host rocks. Both shear zones undergo exhumation during shearing, and we specially relate to the relation between the measured pressure-temperature conditions and the quartz recrystallization events. When applied to majors shear zones, the QSR-metry method highlights across-strike strain rate variations, from 1×10^{-15} s^{-1} in zones where strain is weak, to $>1 \times 10^{-13}$ s^{-1} in zones where it is localized. Strain rates integrated across the shear zones imply fast fault slip rates ~ 1.3 cm yr^{-1} (Karakorum) and ~ 4 cm yr^{-1} (ASRR), proving strong strain localization in these strike-slip continental shear zones.

Keywords

Quartz-strain-rate-metry ; shear zone ; strain localization ; Ailao Shan Red River ; Karakorum ; rheology

1. Introduction

How continental crust and lithosphere absorbs ductile deformations is debated. In particular how far deformation in the middle and deep crust localizes in narrow shear zones or broadly distributed is discussed. Some see the continental crust as coherent blocs separated by fault zones where most of the deformation is absorbed (e.g. Tapponnier et al. [2001]), while others perceive it as a continuous viscous medium where deformation is widely distributed (e.g. Beaumont et al. [2001], Mukherjee [2012]). If GPS studies constrain the short-term repartition of deformation at the surface of the continents, we know less about deeper and longer-term deformations significant for the geological history of continents. This is because even if many theories and descriptions of ductile deformations exist exist (e.g. Ramsay, 1980; Mukherjee, 2013a,b), quantification of their amount and furthermore rate are scarce. Indeed, ductile deformation rates in natural settings have been effectively measured in only three cases [Christensen et al., 1989; Müller et al., 2000; Sassier et al., 2009]. However, Boutonnet et al. [2013] proposed recently a method to measure deformation rates in quartz bearing rocks deformed in the dislocation-creep regime, which could be used in numerous ductile shear zones.

This method, called Quartz-Strain-Rate-metry (QSR), relies both on a piezometer, a flow law calibrated for quartz dislocation-creep recrystallization, and precise measurements of the temperature of deformation [Boutonnet et al., 2013]. Such method was formalized from laboratory experiments that quantitatively describe the properties of quartz at mm scale and at deformation rates of ~10^{-6} s^{-1}. A first set of experiments established piezometer relationships linking the size of recrystallized grains to the applied stress (e.g. Twiss [1977]; Stipp and

Tullis [2003]) while a second set established power flow laws linking the stress to the temperature and the deformation rate (e.g. Hirth et al. [2001]; Gleason and Tullis [1995]; Paterson and Luan [1990]; Luan and Paterson [1992]). However extrapolating from the scale of the experiment to the scale of the natural shear zones is a considerable leap across 8-10 orders of magnitude for the deformation rate, in order to reach the natural values of ~10^{-14} s^{-1}. Furthermore for a given crystal size and a given temperature, results of the QSR vary by five order of magnitude depending on the piezometer and power flow law that are chosen [Jerabek et al., 2007]. In resolve that problem, Boutonnet et al. [2013] performed an empiric calibration of the QSR method using quartz ribbons sampled in an outcrop where the local strain rate had been previously estimated by an independent method [Sassier et al., 2009] and testing different flow laws and piezometers calibrated experimentally. They conclude that the combinations between 1) Hirth et al. [2001]'s flow law and Shimizu [2008]'s piezometer and 2) Paterson and Luan [1990]'s flow law and Stipp and Tullis [2003]'s piezometer lead to correct strain rates measurements in the conditions of deformation of the Ailao-Shan Red-River shear zone (China).

One important prerequisite for QSR method to yield accurate results is to characterize the mechanism of quartz recrystallization and the precise temperature of deformation. Boutonnet et al. [2013] used the TitaniQ thermo-barometer [Wark and Watson, 2006; Thomas et al., 2010] combined with a fluid inclusions study and a previously determined local P-T path as well as Crystallographic Preferred Orientation (CPO) of quartz to constrain the Pressure- Temperature conditions of recrystallization. However, many shear zones exhume during shearing and complicates deciphering precise P-T conditions. Furthermore the ability of the TitaniQ and CPO to accurately constrain the temperature of deformation have been recently challenged (e.g. Grujic et al. [2011]; Kidder et al. [2013]). In this study, we reinvestigate the two shear zones studied in Boutonnet et al. [2013] in order to focus on the quartz recrystallization processes, and discuss the way to accurately constrain the deformation temperature in shear zones undergoing exhumation through time. Finally we discuss the accuracy of the Quartz-Strain-Rate (QSR)-metry, a cheap and fast method allowing generalizing measurements of local strain rates in the continental crust.

2. Methods

Experimental studies show a close relationship (called piezometer) between the average size D of quartz crystals recrystallized during dislocation creep at medium to high temperature and differential stress σ (e.g. Shimizu [2008]; Stipp and Tullis [2003]; Twiss [1977]):

$$\sigma = K\ D^{-p} \qquad (1)$$

where p and K are determined either experimentally or theoretically. The QSR method combines this equation with the ductile rheological law in the same thermodynamic condition, that links the strain rate $\dot{\varepsilon}$, the differential stress σ, the temperature T (e.g. Gleason and Tullis [1995]; Paterson and Luan [1990]; Luan and Paterson [1992]), and in some studies the water fugacity f_{H2O} [Hirth et al., 2001; Rutter and Brodie, 2004]:

$$\dot{\varepsilon} = d\varepsilon/dt = A\ \sigma^n\ f_{H2O}{}^m\ e^{-Q/RT} \qquad (2)$$

where the activation energy Q, the prefactor A, and the exponents n and m are determined experimentally, and R is the ideal gas constant. Combining equations 1 and 2 yields the strain rate $\dot{\varepsilon}$ from the grain size D when the deformation temperature T is known (e.g. Stipp et al. [2002b]).

In most geological contexts, rocks vary in pressure and temperature through time due to burial/exhumation. It is the case for the main strike-slip shear zones of the India-Asia collision zone, where the centre of the shear zones were exhumed during lateral shearing [Leloup et al., 1995, 2001; Boutonnet et al., 2012]. The tricky part of the QSR method is to correlate the measured thermodynamic conditions (T, P and f_{H2O}) with size (D) of quartz grains that recrystallized during shearing. Quartz microstructures have therefore to be studied carefully.

2.1. Quartz microstructures

All samples are pure quartz ribbons, with as little other mineral as possible. Indeed, it has been shown that polymineralic assemblages (quartz + feldspar or micas) approximately follow diffusion creep [Kilian et al., 2011a]. However, the QSR method is based on the use of dislocation creep flow laws, and one has to avoid quartz grains recrystallized in the neighbourhood of foreign minerals. The quartz microstructure was investigated by optical methods in < 30 µm thin sections cut parallel to the lineation (X axis) and orthogonal to the foliation (XZ plane).

The dominant recrystallization mechanisms of quartz is inferred from the type of microstructures, including bulge nucleation (BLG), subgrain rotation (SGR), and grain boundary migration (GBM). These mechanisms often occur in tandem [Hirth and Tullis, 1991; Stipp and Kunze, 2008; Stipp et al., 2002b], but the relative contribution of each mechanism to the bulk microstructure has been demonstrated to vary with stress and/or temperature by laboratory experiments [Hirth and Tullis, 1991] and by observing natural microstructures [Stipp et al., 2002b, a]. Consequently, the recrystallization regimes have long been used to infer temperatures of deformation. The GBM mechanism, characterized by Hirth and Tullis [1991] as regime 3, activate at > 510°C and low stress conditions [Stipp et al., 2002b, a], when there is enough heat energy to allow fast growth of the low-energy grains, those without defects, at the expense of the deformed grains. SGR, described as regime 2 by Hirth and Tullis [1991] is a nucleation regime in which free-energy at the grain boundaries is not high enough to accommodate recovery by boundary migration. Dislocations creep and defects accumulation along crystal planes develop individual subgrains, and then nucleates new grains. This process activates at medium temperature of 400 to 510°C, and medium stress conditions [Stipp et al., 2002b, a]. Bulging (BLG) or local grain boundary migration, described as regime 1 by Hirth and Tullis [1991], is the nucleation regime dominating at low temperature below 400°C and high stress conditions [Hirth and Tullis, 1991; Stipp and Kunze, 2008]. In a recent compilation of natural quartz recrystallization mechanisms, Stipp et al. [2010] also suggested that the transitions amongst these three mechanisms occur at characteristic grain sizes. Finally, the transition between ductile and brittle deformation place the lowest boundary for quartz recrystallization at ~250°C.

2.2. Grain sizes and stress

Quartz boundaries were mapped using quartz lattice preferred orientations measured by Fabric Analyzer (LGGE Grenoble, France). This method identifies the grains by building a map from the <c>-axis (optical axis) orientations. Contiguous pixels with orientation <10-15° misorientation are interpreted to belong to the same grain. Orientation maps with pixel size of 6.8 μm are analysed using ImageJ analysis software (NIH image) and macros developed by the LGGE (Grenoble, France). Grain boundaries are detected and corrected visually to avoid foreign minerals and artefacts. For each grain, we estimate a surface (S, μm^2) and we deduce an equivalent diameter (D, μm) considering each grain as a circle [Stipp et al., 2002a; Stipp and Tullis, 2003]: $D = 2(S/\Pi)^{-2}$. The grain sizes are plotted as frequency histograms, and a Kernell density estimation is calculated. For a single recrystallization event, the size frequency histograms have usually log-normal distributions [Shimizu, 2008; Slotemaker and Bresser, 2006]. For samples with composite microstructures, several log-normal distributions overlap. To distinguish the different grains generations, it is generally accepted that newly recrystallized grains are relatively strain free, whereas older host grains are more internally deformed and contain subgrains. Distributions are analysed with the Past mixture analysis tool [Hammer et al., 2001], which indicates what combination of log-normal distributions produces the best fit of the histogram. The mode(s) of the Gaussian curve(s) is /are the mean grain size. The standard deviation depends on the mean grain size: the higher the mode, the larger the width of the Gaussian curve [Gueydan et al., 2005]. Our size error calculation takes into account the fabric analyser error and a small correction due to the thickness of the grain boundaries, and is approximately on the order of one pixel (6.8 μm).

Paleopiezometry is a relationship linking the dynamically recrystallized grain size formed during dislocation creep and the differential stress [Twiss, 1977]. As most of the piezometers are calibrated for recrystallization regime 2 [Hirth and Tullis, 1991; Stipp and Tullis, 2003; Twiss, 1977; Shimizu, 2008], we select for each sample the quartz grains that correspond to the SGR recrystallization event, based on both the grain size [Stipp et al., 2010] and the microstructure. The grain size analysis is performed on 2D thin sections, implying that the apparent sizes are different than the actual 3D grain size. The relationship between the real grain size (D_3) and the apparent 2D-size (D_2), for spherical grains, can be shown to be: $D_3 = 4/\Pi \times D_2$. In our study the experimental piezometers [Stipp and Tullis, 2003] are calibrated with the 2D value of the grain size, whereas the theoretical piezometers [Twiss, 1977; Shimizu, 2008] are calculated with the 3D value.

2.3. Crystallographic Preferred Orientation

Quartz crystal Crystallographic Preferred Orientation (CPO) describes the orientation of <c>-axis, and sometimes of <a>-axes, of the quartz grains within the ribbon. The CPO indicates the active glide system(s) during deformation and has long been used to infer the type and the temperatures of deformation. For deformation close to simple shear, the activation of the basal plane along the <a> direction, leading to the <c> axis concentrated near the maximum shortening axis (Z axis), is supposed to occur at low temperatures: < 400°C [Gapais and Barbarin, 1986; Stipp et al., 2002a; Passchier and Trouw, 1998]. At higher temperatures, the subordinate activation of the romb-<a> (or rhomb-<a+c>) slip system develops of a girdle in the CPO plots [Menegon et al., 2008; Peternell et al., 2010]. According to Stipp et al. [2002a], the transition from combined basal, rhomb, and prism <a> slip to dominantly prism <a> slip, and therefore from a YZ girdle to a dominant single Y maximum in the <c>-axis pole figures, is rather abrupt and occurs at about 500°C. The temperature range of dominantly prism-<a> slip is between 500°C and ~600 -650°C. This former temperature is that of the onset of dominant prism-<c> slip [Mainprice et al., 1986].

The Fabric Analyser method (Type G50, LGGE, Grenoble), used to measure the CPOs, is a cheap alternative to Electron Back Scattered Diffraction (EBSD), but allows only <c>-axis orientation measurements. We followed a method described by Peternell et al. [2010], based on a stack of eight microphotographs taken with different orientations of the cross-polarized light. The spatial step is 6.8 μm for all samples. The data (colatitudes, azimuth and quality factor) are extracted and their analyses are performed using the package G50

Investigator (http://www.earthsci.unimelb.edu.au /facilities /analyser /downloads.html) and personal Matlab programs. The plots are performed using Stereo32 (http://www.heise.de /download /stereo32-1160507.html). For equigranular quartz ribbons, the <c>-axis repartition is plotted with one point per pixel. However, they are plotted with one point per grain if the quartz sample displays different families of grain sizes.

2.4. The TitaniQ method

The TitaniQ geothermobarometer [Wark and Watson, 2006; Thomas et al., 2010; Huang and Audedat, 2012] is based on the dependence of the chemical substitution between Si^{4+} and Ti^{4+} in Quartz upon pressure and temperature. At high temperatures and high pressures, the number of substituted sites increases [Thomas et al., 2010], leading to the calibration of a thermo-barometer specific to quartz [Wark and Watson, 2006; Thomas et al., 2010; Huang and Audedat, 2012]. It has been proposed that Ti concentrations in quartz can re-equilibrate during dynamic recrystallization at low temperatures [Kohn and Northrup, 2009], despite the very low diffusion rates [Cherniak et al., 2007]. Ti concentrations in quartz are determined by ICP-MS (Element XR) coupled to a laser ablation system (Microlas platform and Excimer CompEx Laser, spot diameters of 33 µm and repetition rates of 10 Hz) at the Geosciences Montpellier (France) and at IUEM Brest (France). Two or three of the Ti isotopes were analysed: ^{47}Ti (7.3% of total Ti), ^{49}Ti (5.5%) and ^{48}Ti (73.8%). The total Ti-content of the sample is calculated averaging Ti-contents estimated from each isotope. The alignment of the instrument and mass calibration is performed before every analytical session using the NIST 612 reference glass. USGS basalt glass reference materials BCR and BIR are used during experiment as standards. Masses isotopes are analyzed over 20 cycles for each analysis. ^{27}Al, ^{29}Si, ^{43}Ca and ^{7}Li isotopes are used to monitor the quartz ablation, and ^{85}Rb, ^{86}Sr and ^{137}Ba to control if other mineral inclusions are also ablated.

Although calibrated for quartz crystallized in the presence of rutile, the thermo-barometer can also be applied to rutile-absent systems if TiO_2 activity is constrained. A Ti activity of ≥0.6 is appropriate for most continental rocks containing a Ti-rich phase (rutile, ilmenite, sphene, biotite) [Wark and Watson, 2006; Ghent and Stout, 1984]. The measurements have been made both in areas where small recrystallized grains are frequent and inside the larger older grains. The Ti-contents of both the centre and the borders of the quartz ribbons were measured in order to check the influence of the matrix, source of Titanium (Figure 1).

3. Geological setting

3.1. The Ailao Shan Red River (ASRR) shear zone

3.1.1. Geological context

The Red River zone is a major physiographic and geological discontinuity in continental East Asia. It stretches for more than 1000 km from eastern Tibet to the Tonkin Gulf, separating the South China and Indochina blocks (Figure 2a), (e.g., BGMRY [1983]; Helmcke [1985]) and possibly extends into the mantle [Huang et al., 2007]. This discontinuity corresponds to at least two different structures: the Red River Fault zone (RRF) and the Ailao Shan Red River shear zone (ASRR). The most recent one is the RRF that shows morphological evidences for recent right- lateral / normal motion [Tapponnier and Molnar, 1977; Allen et al., 1984; Leloup et al., 1995; Wang et al., 1998; Replumaz et al., 2001]. The

RRF straddle along four 10 -20 km wide high-grade metamorphic ranges (Figure 2b): the XueLong Shan, the Diancang Shan, the Ailao Shan and the Day Nui Con Voi. These massifs are interpreted as the exhumed ductile root of the Ailao Shan-Red River (ASRR), that is an Oligo-Miocene left-lateral ductile shear zone (e.g. Tapponnier et al. [1986, 1990]; Leloup and Kienast [1993]; Leloup et al. [1995, 2001]). The metamorphic rocks display a strong ductile deformation, with a generally steep foliation bearing a horizontal lineation. Both parallel the trend of the gneissic cores. Numerous shear criteria indicate that the gneisses are intensively left-lateral sheared (e.g.,Tapponnier et al. [1986, 1990]; Leloup and Kienast [1993]; Leloup et al. [1995]; Jolivet et al. [2001]; Leloup et al. [2001]; Anczkiewicz et al. [2007]).

In the Ailao Shan massif, the shear zone crops out as a ~10 km wide belt of high grade mylonitic gneiss framed by slightly deformed Mesozoic sediments to the north and schists to the south (Figure 2). The shear zone rocks include thinly banded, biotite-sillimanite-garnet-bearing paragneisses, orthogneisses, augengneisses with large feldspar porphyroblasts, migmatites, deformed leucocratic veins, and intrusions of anatectic leucogranites and granodiorites. The paragneisses are found along the northeast side of the range and contain large, up to several tens of meters wide, marbles boudins (Figure 2c). Most rocks are mylonitic but the deformation is more impressive in the paragneiss whilst it could be due to a lack of indicators in the orthogneiss. The RRF bounds the range to the northeast.

Amphibole-rich levels and synkinematic leucocratic dikes are common [Leloup et al., 1995] (Figure 2c). Both of them within their gneissic country rock form spectacular boudins trails that have been used to estimate shear strains [Lacassin et al., 1993; Sassier et al., 2009]. In most outcrops, shear strains are high and all the dikes transpose parallel to the main foliation, and the ductile deformation is difficult to quantify. However, in the orthogneissic core of the Ailao Shan, about 3 km South-West of YuangJiang, the site C1 [Leloup et al., 1995] exhibits various generations of syntectonic dikes. Sassier et al. [2009] determined the strain rate by measuring independently the shear strain (γ) recorded by the dikes and the emplacement age (t) of the same dikes. The minimum strain rates deduced from this study range 3 to $4\times10^{-14}s^{-1}$. This value had been taken as referencto test the different power flow laws and piezometers used by the QSR method [Boutonnet et al., 2013].

The left-lateral shearing occurred under a high geothermic gradient (≥35°C/km), Leloup and Kienast [1993]). The petrologic studies in the Ailao Shan show a metamorphic peak in amphibolite facies conditions (4.5 ±1.5 kbar and 700 ±70°C, Leloup and Kienast [1993]). Left-lateral deformation continued in retrograde, green-schist facies conditions (< 4 kbar and < 500°C, Leloup and Kienast [1993]; Nam et al. [1998]; Jolivet et al. [2001]; Leloup et al. [2001]). Monazite U-Th/Pb dating from the mylonitic fabric and as inclusion within synkinematic garnets constrains the duration of high-temperature metamorphism from 34 to 21 Ma [Gilley et al., 2003]. Felsic and alkaline magmatism, dated from 35 to 22 Ma [Schärer et al., 1994; Zhang and Schärer, 1999], was coeval with both metamorphism and deformation. Considering that left lateral shearing was coeval with cooling, the $^{40}Ar/^{39}Ar$ data constrain the timing of ductile deformation between ~31 and 17 Ma (e.g. Leloup et al. [1995, 2001]). Moreover, Briais et al. [1993] proposed that the South China Sea oceanic basin formed between ~32 Ma and ~16 Ma as a pull apart basin at the Southeast termination of the ASRR implying ~540 km of left-lateral motion along the shear zone. These observations and interpretations have been challenged by some authors. For example Searle [2006] consider that all deformed granites within the ASRR are prekinematic, implying that left-lateral shear started only after 21 Ma (see Leloup et al. [2007]). Other authors questioned the link between motion on the ASRR and sea-floor spreading in the South China Sea (e.g., Clift et al. [1997];

Fyhn et al. [2009]) whilst these studies confirm the existence of a fault linking the ASRR to the spreading centre and the contemporaneity of the two events.

3.1.2. Samples location

We selected nine samples from the Ailao-Shan Red-River Shear zone. Two quartz ribbons have been sampled in the outcrop C1, located in the centre of section C (Leloup et al. [1995], Fig 2c). YY33 and YY35 are both stretching parallel to the main foliation (N120, vertical, lineation pitch: 18°E). YY35 is a cm-wide homogeneous quartz ribbon in a granodioritic gneiss, whereas YY33 displays thin mm-wide quartz ribbons in a hornblende-bearing gneiss. These two samples have been used by Boutonnet et al. [2013] to test and calibrate the QSR method. Three other samples come from the site C2 (Section C, Leloup et al. [1995], Fig.2c), located at the south-western edge of the Ailao Shan massif, bordered by the Ailao Shan fault. YU44 is a large (~5 cm) quartz ribbon, and YU73 and YU42 are thinner (0.5 to 1cm). They lie into the host gneiss composed mostly of black and white micas, quartz and feldspar. YU29 is located in section D, in site D2 (Leloup et al. [1995], Fig 2c). This sample displays a quartz-rich matrix, with feldspar eyes showing sinistral asymmetric deformations, and micas defining the foliation. YY72 and YY54 are located in the north-eastern border of the Ailao Shan massif, near Ejia and between Chunyuan and Gasa respectively. Thin quartz ribbons compose the foliation of the quartz-rich gneisses, oriented N160, 67°E for YY54 and N147, 45°N, with a lineation pitch of 5°S for YY72. Finally, YU61 is a green-hornblende bearing gneiss, with millimetric quartz ribbons, located near YuanYang in the north-eastern border of the south Ailao Shan. YU42, YU44, YU61 and YU29 quartz fabric, measured using a U-stage microscope, have been studied by Leloup et al. [1995]. They showed that YU29 deformed at high temperature, because of the activation of the prismatic

<c> glide system, whereas the three other samples deformed at lower temperatures with activation of both the prismatic <a> and basal <a> glide systems.

3.2. The Karakorum shear zone (KSZ)

3.2.1. Geological context

The NW-SE right-lateral Karakorum fault zone (KFZ) displays a prominent morphological trace from Tash Gurgan in the NW to the Kailash area in the SE (e.g., Weinberg et al. [2000]; Lacassin et al. [2004]). This is related to Quaternary right-lateral motion of the Karakorum fault, which has deflected the course of the Indus river by 120 km [Gaudemer et al., 1989]. However, the rate of recent motion and the active portion(s) of the fault are highly debated, from 1 ±3 mm/yr [Wright et al., 2004] to 11 ±4 mm/yr [Banerjee and Bürgmann, 2002]. Ductilely deformed rocks locally outcrop along the KFZ, (1) in the Nubra valley (Ladakh, India), (2) in the Darbuk Tangtse Pangong region (Ladakh, India) (Fig. 3) and (3) in the Ayilari Range (China). In all these locations the rocks show mylonitic textures with steep foliations and close to horizontal stretching lineations, with unambiguous right-lateral shear criteria (e.g., Lacassin et al. [2004]; Matte et al. [1996]; Phillips and Searle [2007]; Rolland et al. [2009]; Roy et al. [2010]; Searle and Phillips [2007]; Valli et al. [2007]). Because (1) the mylonites are parallel the KFZ for at least 400 km, (2) the mylonites share the same direction and sense of motion as the KFZ, (3) there is no evidence for major tilting of the mylonites after their formation, these mylonites are interpreted as constituting the Karakorum shear zone (KSZ) corresponding to the exhumed deep part of the KFZ.

In the Tangtse zone (34°N, 78.2°E), the KFZ splits into two strands, which flank a topographic range, the Pangong Range, in which slightly deformed to mylonitized magmatic, migmatitic and metamorphic rocks outcrop (Fig. 3a). They constitute a metamorphic belt which exhibit a foliation trending N131 and plunging 84°SE on average, with a stretching lineation dipping from 20° to the SE to 40° to the NW (15° to the NW on average) as previously described (e.g., Jain and Singh [2008]; Phillips and Searle [2007]; Rolland et al. [2009]; Searle et al. [1998]). Shear criteria indicate right-lateral shear. These rocks have been interpreted as the 8 km-wide Karakorum shear zone (KSZ) (e.g., Rolland et al. [2009]; Searle et al. [1998]). The two mylonitic strands which frame the Pangong range are the Tangtse strand to the SW and the Muglib strand to the NE. The exhumation of granulitic rocks (800°C and 5:5 kbar) of the Pangong Range [Rolland et al., 2009], and their rapid cooling, has been related to right-lateral transpressive deformation between the two strands [Dunlap et al., 1998; McCarthy and Weinberg, 2010; Rolland et al., 2009].

Two valleys perpendicular to the belt give access to the structure of the KSZ: the Darbuk valley to the NW and the Tangtse gorge to the SE (Figure 3a). The sections expose from SW to NE: 1) The Ladakh batholith, 2) Rocks belonging to the Shyok suture zone including ultramafics and black mudstones containing Jurassic ammonoid fossils and volcano-clastic rocks [Ehiro et al., 2007]. These rocks are locally intruded by the 18 Ma South Tangtse granite [Leloup et al., 2011]. 3) Mylonites of the Tangtse strand, with dextrally sheared mylonitic ortho- and para-derived gneisses and marbles, and leucocratic dykes parallel to the foliation as well as crosscutting ones. These synkinematic dykes are intruded between 19 and 14 Ma [Phillips et al., 2004; Boutonnet et al., 2012]. 4) The Pangong range where the country rocks and the leucocratic dykes appear less deformed. There, synkinematic migmatisation affects both a metasedimentary sequence comprising Bt-psammites, calc-silicates and amphibolites, and a calcalkaline granitoid suite comprising Bt-Hbl granodiorites, Bt-granodiorites, and diorites [Reichardt et al., 2010]. 5) The Muglib strand with dextrally sheared mylonites, also intruded by synkinematic dykes between 18 and 15 Ma (e.g. Boutonnet et al. [2012]). 6) The Karakorum batholith and the Pangong metamorphic complex (PMC) comprising marbles and large (≤ 10 m) leucogranitic dykes, with foliations trending more easterly than in the KSZ, and locally showing left-lateral shear criteria [McCarthy and Weinberg, 2010]. Note that the various authors give different names to the geologic formations and that we use the names given in Figure 3.

The cooling histories of the four different structural units of the KSZ in the Tangtse area (South Tangtse granite, Tangtse strand, Pangong Range and Muglib strand) have been described by Boutonnet et al. [2012], based on new and published U/Pb and Ar/Ar ages. They showed that the KSZ cooled later that the surrounding terrains. The cooling of the SW side of the shear zone was earlier than its NE side, which is compatible with a reverse fault component of the right-lateral deformation suggested by the NW dip of the lineations in that zone (Figure 3). The time range for right lateral ductile deformation is ≥18.5 to 14 Ma for the South Tangtse mountain, ≥19 to 11 Ma in the Tangtse strand and ≥15 Ma to 7 Ma in the Muglib strand. Combination of the P-T path proposed by Rolland et al. [2009] with the T-t path of Boutonnet et al. [2012] allows building a P-T-t path for the Pangong range unit showing that at least 20 km of exhumation occurred during the right-lateral deformation. About 40% of that exhumation occurred before 12 Ma with a mean rate of 1 mm/yr, while deformation was still ductile. Exhumation of the Pangong range has been attributed to transpressive deformation [Dunlap et al., 1998; McCarthy and Weinberg, 2010; Rolland et al., 2009]. During this exhumation, the apparent geothermal gradient, assumed as linear in the conductive crust, progressively decreased from < 40 °C/km to "normal" geothermal conditions prevailing in an unperturbed lithosphere of 30 °C/km. The initially high geothermal gradient may have been due to heat advection by rising melts or fluids, as suggested by the abundance of granitic magmatism between ca. 20 and ca. 15 Ma [Boutonnet et al., 2012]. The Pangong Metamorphic Complex (PMC), located northeast of the shear zone displays inherited ages from a late Cretaceous metamorphic event at 108 Ma [Streule et al., 2009]. Nevertheless, the PMC has been reheated, possibly by viscous dissipation [Mukherjee and Mulchrone, 2013] and the samples located close to the Muglib strand show clear Miocene cooling ages at 10.6 Ma [McCarthy and Weinberg, 2010].

3.2.2. Samples location

We selected five samples from the Karakorum Shear zone (KSZ), along the Tangtse gorge, joining the village of Tangtse in the southwestern strand of the shear zone to the village of Muglib in the northeastern strand (Fig 3). Sample LA26 is a large quartz ribbon from the deformed part of the South Tangtse granite. This granite, dated at 18.5 ±0.2 Ma by Leloup et al. [2011], is located slightly outside of the shear zone (Fig 3) and is deformed by the Tangtse strand in its northeastern part. As for all samples, the quartz ribbon is parallel to the foliation, trending N120, 65°S in this outcrop. Sample LA30 is a mm to cm-wide quartz ribbon in a matrix of green schist, located in the centre part of the Tangtse strand, within the mylonites (N120, 65°S). The Pangong range is the less deformed part of the shear zone, and the quartz ribbons, formed by quartz segregation during rocks deformation, are rare. LA52 is one of them, taken within the calc-alkaline granodioritic suite. Sample LA59 is a cm-wide quartz ribbon parallel to the weakly deformed schists (N110, 55°N), located few tens of meters South-west of the Muglib strand. LA47 is a thin, ~1mm wide, ribbon of quartz parallel to the main foliation of the Muglib stand mylonites (foliation: N146, 80°S, lineation: pitch 10°SE), composed of fine light schist with clear dextral criteria in this outcrop. Finally, two samples

LA42 and LA44 are located in the Pangong Metamorphic Complex (PMC, Fig 3). In this area, the general foliation turns gradually from ~N110 at ~300m North-East from the Mublig strand (LA44: foliation N105, 75°S, pitch lineation 20°E), to ~N90 at ~500m from it (LA42: foliation N95, 63°S, pitch lineation 19°W). This is interpreted as the deformation of the Cretaceous PMC [Streule et al., 2009] by the dextral movement of the Karakorum Shear zone.

4. Strain rate measurements in natural shear zones

4.1. Recrystallization regime and paleo-stresses

Figure 4 shows the microstructures of our 15 samples, and figure 5 displays their grain size frequency diagrams in logarithmic size and their best normal distributions.

All ASRR samples exhibit completely recrystallized quartz grains in cross-polarized microscopy. Samples YU44, LA73, YU61, YU29, YY33 and YY35 show large grains (1 μm) with boundaries showing lobes amplitude > 20 μm, and irregular shapes and sizes (Fig. 4). In many cases, some grains that appear separated in the 2-D section, have the same crystallographic orientation and actually belong to a common lobbed grain in 3-D. These microstructures are typical of recrystallization mechanism by grain boundary migration (GBM). In all cases, smaller geometric grains are observed at the triple junctions (Fig. 4) and are often associated with zones of undulose extinction and subgrains in the surrounding larger grains. The grains display typically angular shapes with angles close to 120°. This microstructure is typical of an overprinting quartz recrystallization by sub-grain rotation (SGR). As the large (GBM) grains are themselves deformed by processes typical of dislocation migration, we conclude that the SGR event occurred later. In the case of samples

YU29 and YY3, the large GBM-grains are more deformed exhibiting undulose extinction and subgrains, and the SGR-grains are more numerous.

This kind of microstructures typically leads to a bimodal grain size repartition, with a population of large grains corresponding to the GBM ones, and a population of smaller grains corresponding to the SGR event. YU44 and YU73 (site C2) display very similar distributions, with the first mode corresponding to the largest grains population centred at 312.9 ±6.8 and 388.9 ±6.8 μm and the second mode to the smallest grains population centred at 72.2 ±6.8 and 78.2 ±6.8 μm, respectively (Fig. 5). For the two samples coming from site C1 [Boutonnet et al., 2013], the population of largest grains is represented by a first mode centred at 150.4 ±6:8 μm for YY35 and at 127.3 ±6.8 μm for YY33. The second family of grains, represented by the second mode, display sizes at 55.9 ±6.8 and 63.3 ±6.8 μm for these two samples, respectively. The population of large grains of sample YU29 has a mean size of 238.4 ±6.8 μm, and the small grains have a mean size centred at 52.7 ±6.8 μm. Finally, the population of large grains of sample YU61 has a mean size of 167.9 ±6.8 μm, and the small grains have a mean size centred at 61.9 ±6.8 μm. Quartz grains of sample YU42 are large and rather homogenous in colour, size and shape. We measured a log-normal distribution of grain sizes, centred at 92.9 ±6.8 μm. Sample YY54 displays heterogeneous grains, with undulose extinction and subgrains, surrounded by recrystallized grains. This indicates an important recrystallization by sub-grain rotation. Some larger grains have finely lobbed boundaries (~1 - 10 μm, not detected by the Fabric Analyzer). These bulged boundaries are interpreted as a dynamic recrystallization by bulging, for the grains which original orientation did not allow easy dislocation migration [Menegon et al., 2008]. The grain size repartition shows one single mode, centred at 61.6 ±6.8 μm. Finally, sample YY72 displays very elongated and angular quartz grains, typical of a complete recrystallization by subgrain rotation of the rock. The grain size repartition shows one single mode, centred at 36.0 ±6.8 μm.

Six of the seven samples of the KSZ/ PMC area exhibit completely recrystallized quartz grains in cross-polarized microscope whereas sample LA52 shows large quartz grains without dynamic recrystallization and no mean grain size were measured. Samples LA26, LA42, LA44 and LA59 show large lobbed grains typical of grain boundary migration. In the case of LA42, LA44 and LA59, smaller grains are visible, but appear to be lobes of the biggest grains that have been detached to form new grains or could be still attached in 3-D. In sample LA44, two grain size populations were identified, one with very large grains (730.3 ±6.8 µm) and one with smaller grains (107.2 ±6.8 µm). Sample LA59 also shows two populations of grain sizes, with the smallest one centred around 95.2 ±6.8 µm. The grain size repartition of sample LA42 is fitted by a Gaussian curve, indicating a single population, with a mean size of 140.5 ±6.8 µm. The case of sample LA26 is different because the large grains show internal dynamic recrystallization, such as subgrains and undulose extinction, and the small grains, located at triple junctions, are recrystallized by sub-grain rotation (Fig. 4). This dichotomy in microstructures is underlined by the clear bimodal repartition of grain sizes. The population of large GBM grains has a mean size of 223.1 ±6.8 µm and the one of small SGR grains has a mean size of 55.1 ±6.8 µm. Sample LA47 displays also two populations of quartz grains, but the large GBM grains are more deformed and recrystallized and the small SGR grains are more numerous. The mean size of the large grains population is 119.7 ±6.8 µm and the mean size of the small grain population is 31.8 ±6.8 µm. For sample LA30, the SGR recrystallization process is complete. The quartz ribbon displays grains with the same angular shapes with ~120° angles and homogenous sizes well centred around 39.2 ±6.8 µm.

In a context of a shear zone exhumation and cooling, one expects a transition between different recrystallization modes. The GBM-type microstructure is overlaid by the SGR one.

Gueydan et al. [2005] interpret this as a memory of the different phases of exhumation. At high temperature, GBM recrystallization mechanism was active and the whole quartz ribbon recrystallized. During the Ailao Shan massif and the Pangong Range massif exhumation, temperature decreased and SGR recrystallisation mechanism activated below ~500°C, then BLG below ~350°C [Passchier and Trouw, 1998]. The volume proportion of recrystallized grains decreases with temperature. Stipp et al. [2002b] estimate that only 40 and 10% of the volume recrystallize at 500°C and 400°C respectively. The GBM-type microstructure can thus be preserved elsewhere. Only the grain populations of the last recrystallization event, generally by subgrain rotation, are used to calculate a paleo-stress. The results are given in Table 2. For the ASRR, the stresses calculated using Shimizu [2008] piezometer range between 27.8 ±5.3 MPa and 46.8 ±14.6 MPa, and the stresses range between 23.4 ±3.7 MPa and 55.7 ±14.8 MPa [Shimizu, 2008] for the KSZ/PMC area.

4.2. Thermodynamic conditions of recrystallization

4.2.1. CPO results

The CPO analysis of samples YU29, YU61, YY33, YY35 (ASRR), LA42 and LA44 (KFZ) indicate a strong concentration of the <c> axis near the maximum shortening axis (Z axis) (Figure 7). In most cases, the <c> axis fabrics are asymmetrical, and indicate that the basal planes are slightly oblique to the foliation. This geometry is compatible with gliding on the basal plane along the <a> direction under left-lateral simple shear for ASRR and right-lateral simple shear for KSZ (Fig. 7). Moreover, the presence of oblique girdles suggests that some crystals show glide along the <a> direction but on the prismatic planes (Fig. 7). This CPO is consistent with subordinate romb-<a+ c> slip activation. This romb-<a+ c> slip activation is more important in samples YU29 and YU61 (ASRR). For samples YU42, YU44, YU73 (ASRR), LA26 and LA47 (KFZ), the rhomb-<a+ c> glide is accompanied by a maximum of <c> axis concentrated near the intermediate axis (Y axis). This geometry is compatible with gliding principally on the prismatic plane, along the <a> direction. The slight asymmetry of the gliding plane is also consistent with the sense of shearing of the considered shear zone. For samples YY54, YY72 (ASRR), LA30 and LA59 (KFZ), the prism-<a> slip is clearly dominant.

The samples for which a second symmetric girdle appears in CPO plots (e.g. YU73, Fig. 7) indicate that a minor pure shearing component also occurred [Passchier and Trouw, 2005]. In total, therefore a simple shear dominated general shear or sub-simple shear is deciphered. We also noticed that the CPOs are the same for the large grains associated to the GBM recrystallization event and the smaller grains associated to the SGR recrystallization event (see two examples in Figure 6). This indicates that all the quartz crystallographic orientations are consistent with the glide system activated during the last recrystallization event, even the CPOs of the large grains inherited from the GBM recrystallization event.

4.2.2. Titanium-in-quartz measurements

Most of the samples display low values of Titanium-in-quartz (table 1, Figure 8). The lowest value of Ti-content is measured for sample LA42 (KSZ, 1.7 ±0.3 ppm). Then, values around 5 ppm are measured for two samples of the ASRR, YU44 (5:1 0:3 ppm) and YU73 (4.5 ±0.9 ppm), and four samples of the KSZ, LA26 (6.3 ±0.4 ppm), LA30 (4.8 ±0.5 ppm), LA47 (4.3 ±0.5 ppm) and LA59 (4.3 ±0.7 ppm). Applying the thermo-barometer calibration of Thomas et al. [2010], these values, combined with a TiO_2 activity of 0.8 ±0.2, lead to a temperature range of 340 -460°C, for pressures ranging between 0 and 6 kbar (Figures 9 and

10). Intermediate Ti-contents are measured for four quartz ribbon located in the central part of the ASRR: YU42 (10.1 ±2.1 ppm), YY33 (14.6 ±1.8 ppm), YY35 (14.3 ±1.5 ppm) and YU29 (25.9 ±2.1 ppm), leading to a temperature range of 380 – 560°C [Thomas et al., 2010] for pressures ranging between 0 and 6 kbar (Figures 9 and 10). High values of Ti in quartz are measured for the three samples of the north-eastern border of the ASRR: YY72 (40.8 ±4.0 ppm), YY54 (61.7 ±2.9 ppm) and YU61 (64.1 ±8.3 ppm), corresponding to temperatures ranging from 470 to 640°C [Thomas et al., 2010], for pressures ranging between 0 and 6 kbar (Figures 9 and 10).

Slight differences of Ti-contents are observed for YY35 between the quartz vein core (e.g. dd2 to dd6, Fig 1) and the boundaries (dd8, 9 and 11, Fig 1). However this difference could be not significant as it lies within the error bars of the measurements (Fig 8). We observe no difference between core and boundaries Ti-contents for the other samples. Nevertheless, for sample YU73, there is a real difference between the Ti-contents measured in the quartz ribbon (4.8 ±0.7 ppm) and in the matrix (12.1 ±1.9 ppm) (table 1). In most cases, the analyzed points have been made preferentially in the newly recrystallized grains. For control, the Ti-contents of samples YU44 and YU73 quartz veins were investigated for both large and small quartz grains of the quartz vein, and we found no difference between large relict grains and small newly recrystallized grains.

4.2.3. Inferred thermodynamic conditions

The Pressure- Temperature conditions are obtained by combining several thermo-barometers. In the initial calibration of the QSR method (YY35 and YY33) [Boutonnet et al., 2013], the authors intersect two independent thermo-barometers: the TitaniQ and the Fluid Inclusions microthermometry. The results for sample YY35 are displayed in Figure 9a. The conditions of T = 425 ±38°C and P = 130 ±80 MPa are compatible with those of YY33, and are also close to the P-T-time path previously proposed for the central Ailao Shan [Leloup et al., 2001]. The Crystallographic Preferred Orientation of these two samples is consistent with the temperature of deformation. Finally, at 425°C, quartz is supposed to recrystallize by Sub-Grain Rotation [Stipp et al., 2002b]. This suggests that the considered quartz recrystallization event corresponds to the SGR grains and occurred around 23 Ma [Boutonnet et al., 2013]. As the fluid inclusions microthermometry is a tedious method implying one week of work per sample and redundant with the other thermo-barometers, in this study we simply combine the Titanium-in-Quartz thermo-barometer with the local P-T path for the other samples.

Figure 9 presents the pressure- temperature diagrams of the Ailao-Shan Red-River shear zone. The P-T path of the ASRR has been modified in order to fit exactly the P-T conditions given by the site C1 samples. These conditions correspond to a slightly lower pressure than was expected from the central Ailao Shan P-T-t path [Leloup et al., 2001] (Fig. 9a). This is not surprising, as pressure was not tightly constrained in this part of the path [Leloup et al., 2001]. The highest pressure and temperature conditions correspond to the quartz samples located in the north-eastern border of the ASRR: YU61 (P = 180 ±70 MPa and T = 548 ±96°C), YY54 (P = 180 ±80 MPa and T = 544 ±51°C) and YY72 (P = 160 ±80 MPa and T = 507 ±59°C). The samples located close to the centre of the ASRR shear zone display intermediate conditions: YY33/YY35 (P = 130 ±80 MPa and T = 425 ±40°C) and YU29 (P = 150 ±80 MPa and T = 469 ±44°C). Finally, the lowest conditions are recorded by the three samples of site C2, located in the south-western side of the ASRR shear zone: YU42 (P = 120 ±80 MPa and T = 402 ±40°C), YU44 (P = 110 ±80 MPa and T = 367 ±40°C) and YU73 (P = 100 ±80 MPa and T = 352 ±40°C).

Figure 10 presents the Pressure-Temperature diagrams of the Karakorum shear zone. The P-T-t path of the Pangong Range is inferred from the Pressure- Temperature exhumation path of its granulitic unit [Rolland et al., 2009], local P-T conditions in the South-Western strand [Rutter et al., 2007] and the local Temperature- time constrains of Boutonnet et al. [2012]. The P-T-t path of the Pangong Metamorphic Complex is inferred from the studies of Streule et al. [2009] and McCarthy and Weinberg [2010]. Although inherited from a late Createaceous metamorphic event [Streule et al., 2009], the PMC has been reheated during Miocene [McCarthy and Weinberg, 2010] and at least the part of the P-T-t below 500°C is related to the KSZ metamorphic event. All the six samples display rather similar conditions. The pressures are constant around 350 ±80 MPa. The temperatures increase slightly from the north-eastern side to the south-western side: 347 -350 ±50°C in the Pangong Metamorphic Complex (LA42/LA44), 393 -394 ±40°C close to the Muglib strand (LA47 and LA59) and 400 -415 ±40°C in the Tangtse strand (LA30 and LA26). We precise that the P-T conditions of sample LA44 are inferred assuming the same TitaniQ thermo-barometer as sample LA42 located close-by.

5. Discussion

5.1. Constraining the temperature of deformation

Several methods are commonly used to measure the temperature of deformation. They are all disputed, particularly their ability to re-equilibrate when pressure and temperature vary through time. Below, we discuss the accuracy of three methods, and the correlation between the measured thermodynamic conditions and the paleo-stress.

5.1.1. Temperatures deduced from CPOs and recrystallization regimes

The temperature fields inferred from the CPOs and recrystallization regimes have been plotted in Figures 9 and 10 for all samples, following the ranges of temperatures described in sections 2.3 and 2.1. We can notice several inconsistencies. (1) In most cases, the CPO temperatures are higher than the TitaniQ temperatures (e.g. samples LA30, LA59, YU42, YU44, YU73). (2) A more detailed plot of the CPOs for samples showing a clear bimodal grain size repartition indicates that the small grains and the larger grains have the same preferred orientation (Figure 6). (3) Some samples display temperature conditions at which quartz should recrystallize by bulging or GBM, but their sizes [Stipp et al., 2010] and shapes [Stipp et al., 2002b; Passchier and Trouw, 1998] indicate that they recrystallized by SGR. Therefore, we conclude that the temperature ranges inferred from CPOs and recrystallization regimes are sometimes inaccurate because these two phenomena do not depend only on temperature.

Dynamic recrystallization is a very complex process depending on temperature but also stress, strain partitioning into a polymineralic rock and former CPOs.

(1) The influence of stress on recrystallization regimes has long been observed [Hirth and Tullis, 1991; Stipp et al., 2002b] but only recently quantified. The study of Stipp et al. [2010] shows a relationship between the quartz grain size, and thus the stress via a piezometer, and the recrystallization regime. Their results match with our study, in which the populations of grains of the last recrystallization event by SGR have all a 2D-size between ~35 and 120 μm, except sample LA42 (Table 2).

(2) The usual correlation between temperature and CPOs can be locally inverted if a strong phase, like feldspar porphyroclasts, is present into the quartz ribbon [Peternell et al.,

2010]. Therefore, within a polymineralic rock where the deformation is partitioned between minerals, quartz microstructures and CPOs may not represent the bulk rock kinematics [Kilian et al. 2011b]. This should not be the case for our samples, because we chose quartz ribbons as pure as possible (see also part. 5.2.2).

(3) Inherited individual crystals orientations create a kind of strain partitioning. When a quartz crystal has a lattice orientation compatible with the present state of stress, the slip system is easily activated and the grain becomes more elongated with increasing strain [Stipp and Kunze, 2008]. Porphyroclasts with 'hard' orientations, i.e. with an orientation unsuitable for easy slip, are more difficult to deform, and they are selectively removed by dynamic recrystallization [Stipp and Kunze, 2008; Pennacchioni et al., 2010]. This can explain why both populations of the bimodal samples share the same CPO. The large grains are those that were previously favorably oriented, whereas the small newly recrystallized grains derive from prophyroclasts with an initial 'hard' orientation, which recrystallize by SGR to orient more compatibly.

5.1.2. Titanium-in-Quartz temperatures

The TitaniQ thermo-barometer is one of the most precise ways to determine the temperature of quartz: theoretically ±5°C [Wark and Watson, 2006], but practically around ±30°C. This explains why it has been frequently used (e.g. Pennacchioni et al. [2010]; Behr and Platt [2011]) and is the scope of numerous studies (e.g. Cherniak et al. [2007]; Grujic et al. [2011]). The principal question arising from these studies are: (1) how the chemical system behaves during quartz recrystallization? (2) Is the chemical system able to reequilibrate during exhumation?

The distances of diffusional alteration of Ti concentrations in quartz in 1 Ma are approximately 340 µm at 800°C, 10 µm at 600°C, 1 µm at 500°C, and ~0.2 µm at 400°C [Cherniak et al., 2007]. These very slow diffusion rates should greatly limit the applicability of TitaniQ to gauge the deformation temperature, because the duration of plastic shearing along a ductile shear zone is usually not sufficient at T < 600°C to homogeneously reset the Ti concentration in quartz grains > 10 µm. Nevertheless, several recent studies [Grujic et al., 2011] showed that the Ti-diffusion processes may be enhanced at temperatures as low as ~500°C by the fast grain boundary movements during GBM recrystallization in presence of water. Kidder et al. [2013] extended this to temperatures as low as 250 – 410°C, at which quartz recrystallize by slow boundary migration through bulging, but they found that the calibration of Huang and Audedat [2012] is more accurate in these conditions. Consequently, in a pure Sub-Grain Rotation regime, one does not expect an efficient Ti reequilibration into quartz. Moreover, several authors [Stipp et al., 2002a; Behr and Platt, 2011] showed that quartz can keep in memory inherited temperatures: large porphyroclasts generally give much higher Ti concentrations than the surrounding recrystallized grains and this difference is interpreted as low stress/ high temperature former conditions kept in memory by the large non-recrystallized grains, and a Ti-reequilibration for newly recrystallized grains [Kohn and Northrup, 2009; Spear and Wark, 2009]. Thus, during cooling, the TitaniQ temperatures should either be inherited high temperatures (> 500°C) [Stipp et al., 2002a; Behr and Platt, 2011; Grujic et al., 2011] or temperatures close to the ductile- brittle transition (< 400°C).

However, our temperatures ranging between 350°C and 550°C (Table 2), indicate that Ti-contents in quartz reequilibrated during recrystallization by SGR. Moreover, large grains and small grains display similar Ti-contents. We propose two hypotheses to explain these observations. Hypothesis (1) is related to the fact that most of the studies dealing with the behaviour of the Titanium substitution in quartz are made either in steady-state conditions or during prograde metamorphism [Grujic et al., 2011]. Negrini et al. [2014] proposed that the retrograde exsolution of Titanium is much easier than its prograde incorporation into quartz. This can explain why quartz reequilibrated at medium temperatures in both the ASRR and the KFZ, that both underwent a retrograde evolution during shearing. Hypothesis (2) is related to the fact that most of the studies (e.g. Hirth and Tullis [1991]) consider that the three recrystallization regimes are independent and activated at different stress/ temperature conditions. Another theory associate a nucleation process to a growth process [Derby and Ashby, 1987; Shimizu, 2008]. In their models, the average grain size is derived from a dynamic balance between nucleation, which reduces the grain size, and grain growth. For our samples, the nucleation process is SGR and the growth process is GBM. The relative contribution of each mechanism to bulk microstructure varies with stress and temperature [Hirth and Tullis, 1991; Stipp et al., 2002b]. Therefore, the small contribution of grain boundary migration at medium temperatures could be sufficient to re-equilibrate the Ti.

Despite all the questions related to the TitaniQ thermo-barometer, we consider the measured P-T conditions as reliable because they are all consistent with the last recrystallization event, leading to the development of the smallest population of grains. Therefore, this thermo-barometer is used to infer the temperature of deformation because it re-equilibrates during retrograde exhumation, as long as quartz recrystallize, and it closes during/ just after the last recrystallization. The other ways to measure the temperature of deformation in quartz, as CPOs and microstructures, are less precise and depend too much on other parameters, such as stress, to be used for the QSR method.

5.2. Strain rates measurements

5.2.1. Strain rates of ASRR and KFZ shear zones

The strain rates of some samples have already been measured in a previous study [Boutonnet et al., 2013], but the grain sizes were measured using cross-polarized micrographs. In this study, we used a more robust method, with grain boundary maps based on the <c>-axis orientations. The results are given in Table 2 and are close of the previous ones. Boutonnet et al. [2013] showed that, among all piezometers and flow laws calibrated for quartz, only few combinations of them give accurate strain rates: (1) Stipp and Tullis [2003] experimental piezometer corrected for an experimental bias [Holyoke and Kronenberg, 2010] yields satisfactory results when associated with Paterson and Luan [1990] flow law and (2) Shimizu [2008] theoretical piezometer gives accurate results when combined with Hirth et al. [2001] flow law. The strength of the first combination is the use of the only experimental piezometer calibrated for quartz [Stipp and Tullis, 2003]. The strength of the second one is the use of the only flow calibrated both on experimental and natural samples [Hirth et al., 2001], and taking into account the water fugacity (f_{H2O}). The water fugacity can be assimilated to the hydrostatic pressure, calculated knowing the Pressure (P, MPa) and a fugacity coefficient, C, determined experimentally and depending on both pressure and temperature [Tödheide, 1972]: $f_{H2O} = P \times C$ (Table 2).

The calculated strain rates range between 1.1 $\times 10^{-15}$ s^{-1} and 2.0 $\times 10^{-12}$ s^{-1} for the ASRR shear zone, using the piezometer of Shimizu [2008] and the flow law of Hirth et al. [2001] (Table 2, Fig. 11). The combination between Stipp and Tullis [2003]'s piezometer and Paterson and Luan [1990]'s flow law provides very close strain rates, with highest error bars due to the error on the experimental calibration of Stipp and Tullis [2003]'s piezometer. The highest values (> 5 $\times10^{-13}$ s^{-1}) correspond to samples located close to the north-eastern border of the shear zone (YU61, YY54 and YY72) and the lowest values (< 5 $\times10^{-15}$ s^{-1}) to samples located close to its south-western border (YU42, YU44, YU73). The samples in the centre of the shear zone display intermediate values (YU29, YY33, YY35) (Fig. 11a). Plotting the strain rates in linear scale highlights the fact that most of the deformation was absorbed by the mylonitic strand located close to the Red-River fault.

The calculated strain rates range between 6.3 $\times10^{-16}$ s^{-1} and 2.7 $\times10^{-13}s^{-1}$ for the Karakorum shear zone, using the piezometer of Shimizu [2008] and the flow law of Hirth et al. [2001] (Table 2, Fig. 11). The combination between Stipp and Tullis [2003]'s piezometer and Paterson and Luan [1990]'s flow law provides lower strain rates, with half an order of magnitude of difference. This difference between the results of the two combinations is higher for the KSZ than forthe ASRR, where the initial calibration was made [Boutonnet et al., 2013]. This happened since the confining pressure is higher for the KSZ (ca. 350 MPa) than that for the ASRR (ca. 150 MPa). This difference of confining pressure is taken into account by Hirth et al. [2001]'s flow law through thewater fugacity parameter, whereas it is ignored by Paterson and Luan [1990]'s flow law. For this reason, we prefer to rely to the strain rates provided by the combination Shimizu [2008]'s piezometer / Hirth et al. [2001]'s flow law. For the KSZ, the highest values (> 1 $\times10^{-13}$ s^{-1}) correspond to samples located in the two mylonitic strands (LA30 and LA47). Intermediates values (around 1 $\times10^{-14}$ s^{-1}) are obtained for samples located close (< 200m) to these mylonitic strands (LA26 and LA59). Finally, the lowest values (≤ 1 $\times10^{-15}$ s^{-1}) correspond to samples located far from the mylonitic strands, either in the centre of the shear zone (LA52) or outside of it (LA42/LA44). For sample LA52, a very low strain rate value is inferred from the nearly non deformed quartz, where no dynamic recrystallization could be identified (Fig. 4).

5.2.2. Quartz rheology vs. bulk rock rheology

We ensured that, at the scale of the quartz ribbon, quartz recrystallized freely by dislocation creep mechanism. As mentioned in section 2.1, the purity of the quartz ribbon is important because foreign minerals can vary stress locally and partition strain [Stipp and Kunze, 2008; Peternell et al., 2010]. We evaluated the effect of strong phases such as feldspar. We sampled a quartz ribbon (LA33) in which feldspar phenocrysts are present, within the mylonitic gneiss of the Tangtse strand of the KSZ located ~100m from sample LA30. Figure 12 shows the <c>-axis orientations measured by Fabric Analyzer method. The feldspar prophyroclasts define pressure shadows, compatible with the dextral sense of shear. Inside the pressure shadows (Fig. 12), the recrystallized quartz grains are larger than elsewhere, and their CPOs rotated by an angle of ~30° compared to the CPOs outside of the pressure shadows. The CPOs outside of the pressure shadows resemble to those of the pure quartz ribbon LA30 located in the same area (Fig. 7). Thus, the local stress variations induced by the presence of strong prophyroclasts disturb quartz recrystallization and can induce errors in the QSR method.

It has been shown that micas aligned in continuous layers / foliations impart strain weakening [Park et al., 2006]. Consequently, dynamic recrystallization of quartz modify at the contact of phyllosilicates. In most of gneissic rocks where the quartz ribbons are sampled, the matrix consits of a mixing of quartz, feldspar and micas, and one must avoid all measurements of grain size at the edges of the quartz ribbons. Finally, polymineralic assemblages (quartz + feldspar or micas) behave with a rheological law close to the diffusion creep one [Kilian et al., 2011a], whereas the QSR is based on dislocation creep laws.

For all these reasons, the QSR method should be applied in pure quartz ribbons. Few of our samples show small feldspars (YU29, YY33, YU61 and YY72, Figure 4), but they are so elongated that we noticed no alteration of the shape and orientation of quartz around them.

At the scale of the sample, one has also to make sure that the quartz ribbon represents the bulk rheology. All our quartz ribbons from the ASRR and KFZ are formed by mineral segregation during deformation. If applied to a late quartz vein, even deformed, the QSR method would not constrain the rheology of the host rock. In this study, we selected quartz ribbons parallel to the main foliation, and we checked with the CPOs that the shear sense is compatible with that of the shear zone (Fig. 7). Handy [1990] described three end-member types of mechanical and microstructural behavior for polymineralic rocks: (1) strong minerals form a load-bearing framework that contains spaces filled with weaker minerals; (2) two or more minerals with low relative strengths control bulk rheology and form elongate boudins; (3) one very weak mineral governs bulk rheology, while the stronger minerals form clasts. Our gneissic samples (all ASRR samples and LA26 from KSZ) typically belong to group 2, with a phase of pure quartz, and a phase composed of a homogeneous mixing of micas, recrystallized quartz and recrystallized feldspar. Both phases form elongated layers parallel to the foliation, indicating that they both control the bulk rheology. For the quartz ribbons surrounded by a schist matrix (all KSZ samples, except LA26), the phyllosilicate-rich layers can control the bulk rheology. However, when the difference of strength between the two phases is significant, the strong phase should form clasts and not ribbons [Mancktelow and Pennacchioni , 2010]. This indicates that even in the case of a schist matrix, the polymineralic rock deforms mostly in regime 2, and the measured strain rate represents the bulk rock strain rate.

5.3. Method limitations

Samples LA42 and LA44 (KSZ) illustrate well some limitations of the QSR method. First is the minimum deformation rate needed to recrystallize quartz. The lowest value of strain rate measured by the QSR method in this study is 6.3×10^{-16} s^{-1} (LA42 -KSZ). The strain rates value of this sample is to take with care, because neither the shape nor the size [Stipp et al., 2010] of the recrystallized grains allowed us to be sure that they recrystallized by subgrain rotation (Table 2): in this case, applying the QSR method calibrated for subgrain rotation could be not adequate. For sample LA44, the strain rate is also not well constrained because no TitaniQ temperature was measured and we took the P-T values of the nearby sample LA42. A value of ~1×10^{-15} s^{-1} seems to be the lowest limit of strain rate that can be measured precisely by QSR-metry. Second, these two samples are taken outside of the Karakorum Shear Zone, in the Pangong Metamorphic Complex, a range metamorphized and deformed during the late Cretaceous [Streule et al., 2009], and reheated by the KSZ during the Miocene [McCarthy and Weinberg, 2010]. Nevertheless, no clear dextral deformation can be inferred from the CPOs (Figure 7), and the correlation between the temperature (T) and the deformation (σ) is not obvious. In that case, the calculated strain rate ($\dot{\varepsilon}$) with the QSR method could be inaccurate. The only assertion we can make is that, during Miocene, the strain rate was lower than 1×10^{-15} s^{-1} at ~300m northeast from the Mublig strand.

Considering the temperature and grain size uncertainties, as well as those of the piezometers and flow laws, yields relatively large error bars on the final result (Fig. 11, Table 2), the main error source being the uncertainty on the deformation temperature [Boutonnet et al., 2013]. The error bars in strain rates are generally of the order of magnitude in log-scale, which has to be taken into account when absolute values are calculated. But the QSR method is robust when relative values are compared. In both our cases, train rates are obviously inhomogenous across the shear zones.

5.4. Strain localization across shear zones

By using the QSR method calibrated by Boutonnet et al. [2013], we address the problem of localization of the deformation on two major shear zones, for which both fast and slow fault slip rates have been proposed (Fig. 11).

The Miocene slip rate of the 10km- wide ASRR shear zone has been suggested to be to be rather fast, between 2.8 and 5.3 cm yr^{-1} using geological markers, plate tectonic reconstructions, and cooling histories (e.g., Leloup et al. [2001]), or conversely to be slower than 1.4 cm yr^{-1} using different geological markers (e.g., Clift et al. [1997]). If deformation was homogeneous in space and time within a 10-km wide shear zone, this would correspond to shear rates between 8.9×10^{-14} s^{-1} and 1.7×10^{-13} s^{-1}, or below 4.4×10^{-14} s^{-1}, respectively. When plotted along a cross section of the shear zone, the measured strain rates show a progressive increase from 1.1×10^{-15} s^{-1} in the southwest to 2.0×10^{-12} s^{-1} in the northeast (Fig. 11), that can be approximated as a linear increase of $\log(\dot{\varepsilon})$. This suggests strong deformation localization along the northeast border of the shear zone, assuming that quartz represents the rock rheology (see section 5.2.2).

According to the local P-T-t paths of the ASRR (Fig.9), all the recrystallization used for QSR-metry occurred coevally, around 22 ±1 Ma (Figure 9). In the center of the shear zone (site C1), Sassier et al. [2009] showed that ductile deformation ceased just after the youngest 22.55 ±0.25 Ma dike emplaced. In the North-Eastern border of the shear zone, left-lateral, strike-slip ductile deformation probably ceased by about 20 Ma, followed by the activation of the normal brittle Red River Fault [Harrison et al., 1992]. Thus the considered recrystallization events correspond to the very last moments of ductile deformation. An integrated fault slip rate on the order of 4 cm yr^{-1}, valid at ~22 ±1Ma, is calculated across the shear zone. Such velocity is in the high range of the slip rates proposed for the ASRR.

The differential stresses according to Equation 1 range 28 - 47 MPa (Shimizu [2008] piezometer), and the temperatures range 350°C - 550°C. The correlation between local temperatures and local strain rates is clear, with the lowest temperatures recorded in the south-western side and the highest ones in the north-eastern part (Table 2, Figure 2). So, strain localization across the ASRR at ca. 22 Ma seems to be controlled mostly by the local temperatures.

The Neogene- Quaternary slip rate of the Karakorum Fault Zone is disputed, with values deduced from geological and geodetic data range <0.5 cm yr^{-1} up to 1.1 cm yr^{-1} (e.g., Wright et al. [2004]; Chevalier et al. [2005]; Boutonnet et al. [2012]). In the Tangtse area (India), deformation confined within the two narrow Tangtse and Muglib mylonitic strands (e.g., Boutonnet et al. [2012], Fig. 3). The six QSR measurements confirm this impression with values above 1.6×10^{-13} s^{-1} in the two mylonitic strands, and below 1.0×10^{-14} s^{-1} outside (Fig. 11). This suggests that strain localized in the two mylonitic strands, as suggested by the qualitative description [Boutonnet et al., 2012], assuming once more that quartz represents the rock rheology (see section 5.2.2). The measured shear rates correspond to an integrated fault slip rate of 1.3 cm yr^{-1}, in the highest range of the previous geological and geophysical estimates.

According to the local P-T-t paths of the KSZ (Fig. 10), all the recrystallization events used for QSR-metry occurred at the same temperature, 380 ±35°C, slightly above the ductile-brittle transition located at ~10km depth (Boutonnet et al., 2012). As in the ASRR case, these recrystallization events correspond to the very last moments of ductile deformation. A diachronism of cooling ages is observed across the shear zone: ductile deformation ended at ~12 ±1Ma in the Tangtse strand and 8.5 ±0.5 Ma in the Muglib strand [Boutonnet et al., 2012]. As no evidence of brittle deformation had been found in the Tangtse strand, we suggest that ductile deformation finally localized in the Muglib strand after 10 Ma, and that deformation became brittle when temperature became too low, as attested by the occurrence of brittle faults [Rutter et al., 2007].

According to Equation 1 and Shimizu [2008], the differential stresses range between 24 and 67 MPa, at a rather constant temperature (380 ±35°C) across the shear zone. The highest stresses are recorded in the two mylonitic strands, especially in the Muglib strand, where brittle deformation finally localized. Thus, strain localization across the KSZ between 13 and 8 Ma seems to be associated to high stresses rather than temperature differences.

In the case of the ASRR and Karakorum shear zones, deformation rates appear to be variable across strike, with narrow (a few kilometres wide) zones with strain rates of $\geq 10^{-13}$ s^{-1} where most of the deformation localizes. This is in accordance with the qualitative field observations. For the two studied cases, the shear rates, when integrated across strike, are compatible with the fastest slip rates inferred from geologic and geodetic considerations. The strain rates in these kilometre-wide zones are more than 500 times higher than in the other parts of the exposed shear zones, and more than 1000 times higher than in the shear zone surroundings. This implies that a 1-km-wide zone of localized strain can accommodate as much deformation as a 1000-km-wide block. The temperature is often proposed to be the major cause of strain localization (e.g. Leloup et al. [1999]), which seems to be the case in the ASRR shear zone at the end of its ductile history. Nevertheless, the strain localization in the

Karakorum shear zone seems to be related to high stresses, which can themselves result from grain size reduction (e.g. Ricard and Bercovici [2009]; Rozel et al. [2011]).

6. Conclusions

The QSR method provides measurements of local strain rates, in terms of time and space, of ductilely deformed continental rocks. As quartz is one of the most ubiquitous mineral in continental crust, the measurements could be rather dense, provided that deformation is intense enough to recrystallize the quartz layers. Thus, a regular sampling of quartz ribbons should allow mapping the strain rate across or along a natural shear zone at a given moment of its history. Because of recent improvements of several methods that can be efficiently used for quartz measurements, such as the TitaniQ method [Wark and Watson, 2006] or the Fabric Analyzer for the CPOs [Peternell et al., 2010], the QSR-metry method is rather fast and cheap. The quartz recrystallization regime and grain size are inferred from optical observations and Crystallographic Preferred Orientations measurements. We combine the TitaniQ thermo-barometer [Thomas et al., 2010] to the local Pressure- Temperature-time path of the shear zone in order to measure the thermodynamical conditions of the last recrystallization event. The accuracy can be improved by the use of the quartz Fluid Inclusions Microthermometry [Boutonnet et al., 2013], but the time to analyze each sample is much longer.

Nevertheless, several pitfalls are to be avoided: (1) in a context where pressure and temperature vary through time, such as during exhumation, a careful correlation between the different parameters (grain size, temperature, pressure) has to be done; (2) quartz has to recrystallize freely, without interference with other minerals in pure quartz ribbons, and in a matrix of same strength, so that the quartz rheology represents the bulk rock rheology.

The obtained strain rates can be plotted on sections across strike and compared relatively. In the case of the Ailao Shan- Red River shear zone, strain localization occurs in the north-eastern side of the shear zone, and for the Karakorum shear zone, two lateral strands localize mostly the ductile deformation before the transition to brittle deformation. The quantitative results of strain localization agree with the field observations of mylonites localization. Moreover, despite the large error bars, the absolute shear rate, integrated across the entire shear zone, agree with longer term geological measurements. The two studied ductile shear zones thus localize large amounts of deformation.

Stress and strain rate profiles obtained through this method can be a reference for experimental studies, in order to test the main rheological laws and the piezometers, in real conditions. Indeed, most of the experimental studies are made at strain rates much higher than the natural ones (~8 orders of magnitude) and few experimental studies take into account the burial or exhumation processes. Finally, these profiles can be useful as a benchmark for numerical studies that deal with the strain localization inside shear zones (e.g. Leloup et al. [1999]).

Acknowledgments. We thank the French National Program 3F (INSU -CNRS) for funding. Emmanuelle Boutonnet thanks the ERC 258830. We are grateful to V. Gardien, C. Lefebvre, M. Montagnat, M. Peternell, Y. Ricard, C. Sassier, and K. Schulmann for discussions and advice. We thank Petr Jeřábek and Soumyajit Mukherjee for constructive reviews.

Figures captions

Figure 1:

Location of the laser ablation spots for samples YY35 and YU44. : point X_n corresponds to data dd_n of Fig. 8. The Ti-contents of both the center and the borders of the quartz ribbons were measured in order to check the influence of the matrix (Ti-source).

Figure 2:

Geological maps and sections of Ailao Shan Red River (ASRR) shear zone. (a) Location of the major strike-slip shear zones in the India- Asia collision zone. RRF : Red River fault, KuF : Kunlun Fault, ATF : Altyn Tagh Fault, KF : Karakorum fault, SF : Science Fiction. (b) Simplified geological map of the ASRR shear zone. Modified after Leloup et al. [2001] and Sassier et al. [2009]. (c) Geological cross-sections C and D of Ailao Shan metamorphic range in Yuanjiang region, with sites C1, C2 and D2 location. Modified after Leloup et al. [1995]. A.F.: Ailao Shan Fault ; R.F.F. = active Range Front Fault (mainly normal slip) ; M.V.F. = active Mid Valley Fault (purely strike slip).

Figure 3:

Geological map and section of the Karakorum shear zone (KSZ). The general location of the KSZ is given in Figure 2a. (a) Simplified geological map of the KSZ in the region of Tangtse (India), and (b) its corresponding SW-NE directed geological cross-section, modified after Leloup et al. [2011] and Boutonnet et al. [2012]. All the studied samples are located, as well as the main structures orientations. PMC: Pangong Metamorphic Complex.

Figure 4:

Quartz microstructures. <c>-axis orientations images of 9 samples of the ASRR (YU and YY) and 7 samples of the KSZ (LA) or the Pangong Metamorphic Complex (PMC), obtained by Fabric Analyzer method. The thin sections are cut in the XZ plane, parallel to lineation and normal to foliation (view from above). The colour code of the <c>-axis orientation is given in a stereographic plot (lower hemisphere). Large grains with amoeboid shapes, irregular and lobbed boundaries are interpreted as recrystallized by grain boundary migration. Small regular-shaped grains, spatially link to sub-grains, are interpreted as sub-grain rotation recrystallization mechanism. These pictures are used to map the grain boundaries.

Figure 5:

2-D quartz grain size distribution for 9 ASRR samples (YU and YY) and 6 KSZ samples (LA). The X-scales are in logarithmic scale of the size (μm). The best mixture of normal distributions that could drive to each frequency histogram is calculated. When a bimodal repartition is preferred, the dashed line represents the large grains, and the continuous line represents the smaller grains, which size (indicated, in μm) is taken for the stress calculation. The results are reported in Table 2. BLG : Bulging ; SGR : Subgrain Rotation ; GBM : Grain boundary migration. The size fields of recrystallization mechanisms are defined by Stipp et al. [2010].

Figure 6:

Comparison of the CPOs of bulk quartz ribbon (left) and newly recrystallized quartz grains (right). Up: sample YY35 (ASRR). Down: sample LA26 (KSZ). Small grains belonging to the last recrystallization event are indicated with white squares on CPO maps (left).

Figure 7:

Quartz CPO of samples from the ASRR and Karakorum shear zones. The CPOs are obtained from Fabric Analyzer method. The plots are stereographic lower hemisphere projections, with cosine density contours.

Figure 8:

Titanium-in-quartz measurements by La-ICP-MS. ^{47}Ti, ^{49}Ti and ^{48}Ti (when available) contents of quartz (ppm) for each analyse (dd_n), and weighted average for all isotopes. No remarkable difference is noticed between core and rim analysis in sample YY35 and YU44 quartz veins - see Figure 1. For sample YU73, only the quartz vein data are plotted and not the quartz matrix ones. All the data are presented in Table 1 and Table 2.

Figure 9:

Correlation between P-T-t conditions of quartz equilibration and recrystallization events for the ASRR. The temperature conditions are given by the intersection between the TitaniQ thermo-barometer for quartz and the local P-T-t fields [Leloup et al., 1995, 2001; Harrison et al., 1992, 1996]. The ranges of temperatures deduced from microstructures [Stipp et al., 2002b, a] and CPOs [Gapais and Barbarin, 1986; Stipp et al., 2002a; Mainprice et al., 1986] are also plotted even if discussed (see section 5.1.1).

Figure 10:

Correlation between P-T-t conditions of quartz equilibration and recrystallization events for the KSZ. The temperature conditions are given by the intersection between the TitaniQ thermo-barometer for quartz and the local P-T-t fields [Boutonnet et al., 2012; Rutter et al., 2007; Rolland et al., 2009; McCarthy and Weinberg, 2010]. The ranges of temperatures deduced from microstructures [Stipp et al., 2002b, a] and CPOs [Gapais and Barbarin, 1986;

Stipp et al., 2002a; Mainprice et al., 1986] are also plotted even if discussed (see section 5.1.1).

Figure 11:

Sections across two major shear zones showing the local strain rates (Boutonnet et al. [2013], modified). The quartz-strain-rate-metry (QSR) method used the Shimizu [2008]/ Hirth et al. [2001] piezometer rheological/ flow law pair (black dots) and the Stipp and Tullis [2003]/ Paterson and Luan [1990] piezometer rheological/ flow law pair (grey dots). A: Ailao Shan - Red River (ASRR; south-west China) shear zone (see Fig. 1B). Bulk strain rates are calculated for a 10-km-wide shear zone, respectively inferring fast fault slip rates between 2.8 and 5.3 cm/yr (red), or slow ones between 0.5 and 1.4 cm/yr (blue). B: Karakorum shear zone (KSZ, India), at the latitude of Tangtse village. Bulk strain rates are calculated for a 8-km-wide shear zone, respectively inferring fast fault slip rates between 0.7 and 1.1 cm/yr (red), or slow ones between 0.1 and 0.5 cm/yr (blue). Open symbols correspond to samples, for which the strain rates are not well constrained (LA42, LA44 and LA52). Up: log-scale vertical axis; Down: Linear-scale vertical axis. Sc -schist, M -mylonites, Se -sediments, G -undeformed granite, Me -metamorphic, PMC -Pangong Metamorphic Complex, str. -strand. Dot-dashed lines indicate shear rate profiles used for the calculation of the integrated shear rates.

Figure 12:

Example of strain partitioning. Sample LA33 is located close to LA30 (see Figure 3) but quartz recrystallization is disturbed by the presence of strong feldspars. Left: stereographic plots of Crystallographic Preferred Orientation of quartz <c>-axis, far from the prophyroclasts (up) and in the pressure shadows (down). Density calculation: Cosine sums. Corsine exponent = 20. Contour intervals = 10. From minimum to maximum. Equal angle projection, lower hemisphere. Right: map of quartz <c>-axis CPOs (up) with corresponding color code, and corresponding natural light micrography of the quartz ribbon (down), with location of Feldspars and pressure shadows during dextral shearing.

Tables titles

Table 1:

Titanium-in-quartz measurements.

Table 2:

QSR strain rate measurements in the ASRR and KFZ strike-slip shear zones.

References

Allen, C. R., A. R. Gillespie, Y. Han, K. E. Sieh, B. Zhang, and C. Zhu (1984), Red river and associated faults, Yunnan province, china: Quaternary geology, slip rates and seismic hazard, Geological Society of America Bulletin, 95, 686- 700, doi: 10.1130/0016-7606(1984)95.

Anczkiewicz, R., G. Viola, O. Mutener, M. F. Thirlwall, I. M. Villa, and N. Q. Quong (2007), Structure and shearing conditions in the day nui con voi massif: Implications for the evolution of the red river shear zone in northern vietnam, Tectonics, 26(2), TC2002, doi: 10.1029/2006TC001972.

Banerjee, P., and R. Bürgmann (2002), Convergence across the northwest himalaya from GPS measurements, Geophysical Research Letters, 29(13), 30-1–30-4, doi: 10.1029/2002GL015184.

Beaumont, C., R. A. Jamieson, M. H. Nguyen, and B. Lee (2001), Himalayan tectonics explained by extrusion of a low-viscosity crustal channel coupled to focused surface denudation, Nature, 414(6865), 738-742, doi: 10.1038/414738a.

Behr, W. M., and J. P. Platt (2011), A naturally constrained stress profile through the middle crust in an extensional terrane, Earth and Planetary Science Letters, 303(3-4), 181-192, doi: 10.1016/j.epsl.2010.11.044.

BGMRY (1983), Geological map of Yunnan. Bureau of geology and mineral resources of yunnan, 1:500000.

Boutonnet, E., P. H. Leloup, J. L. P. N Arnaud, W. J. Davis, and K. Hattori (2012), Synkinematic magmatism, heterogeneous deformation, and progressive strain localization in a strike-slip shear zone: The case of the right-lateral karakorum fault, Tectonics, 31, TC4012, doi:10.1029/2011TC003049.

Boutonnet, E., P. H. Leloup, C. Sassier, V. Gardien, and Y. Ricard (2013), Ductile strain rate measurements document long term strain localization in the continental crust, Geology, 41, 819-822, doi:10.1130/G33723.1.

Briais, A., P. Patriat, and P. Tapponnier (1993), Updated interpretation of magnetic anomalies and sea floor spreading stages in the south china sea, implications for the tertiary tectonics of SE asia, Journal of Geophysical Research, 98(B4), 6299-6328, doi: 10.1029/92JB02280.

Cherniak, D., E. Watson, and D. Wark (2007), Ti diffusion in quartz, Chemical Geology, 236(1-2), 65-74, doi:10.1016/j.chemgeo.2006.09.001.

Chevalier, M.-L., F. Ryerson, P. Tapponnier, R. Finkel, J. V. D. Woerd, L. Haibing, and L. Qing (2005), Slip-rate measurements on the Karakorum fault may imply secular variations in fault motion, Science, 352(307), 411-414, doi: 10.1126/science.1105466.

Christensen, J. N., J. L. Rosenfeld, and D. J. DePaolo (1989), Rates of tectonometamorphic processes from rubidium and strontium isotopes in garnet, Science, 244, 1465-1469. doi: 10.1126/science.244.4911.1465.

Clift, P. D., H. V. Long, R. Hinton, R. M. Ellam, R. Hannigan, M. T. Tan, J. Blusztajn, and N. A. Duc (1997), Evolving east asian river systems reconstructed by trace element and Pb and Nd isotope variations in modern and ancient red river-song hong sediments, Geochem. Geophys. Geosyst, 9(4), doi:Q04039, doi:10.1029/2007GC001867.

Derby, B., and M. Ashby (1987), On dynamic recrystallization, Scripta Metallurgica, 21(6), 879-884, doi: 10.1016/0036-9748(87)90341-3.

Dunlap, W., R.Weinberg, and M. Searle (1998), Karakorum fault zone rocks cool in two phases, Journal of the Geological Society, 155, 903-912, doi: 10.1144/gsjgs.155.6.0903.

Ehiro, M., S. Kojima, T. Sato, T. Ahmad, and T. Ohtani (2007), Discovery of jurassic ammonoids from the shyok suture zone to the northeast of chang la pass, ladakh, northwest india and its tectonic significance, Island Arc, 16, 124-132, doi: 10.1111/j.1440-1738.2007.00562.x.

Fyhn, M. B. W., L. O. Boldreel, and L. H. Nielsen (2009), Geological development of the central and south vietnamese margin: Implications for the establishment of the south china sea, indochinese escape tectonics and cenozoic volcanism, Tectonophysics, 478(3-4), 184-214, doi: 10.1016/j.tecto.2009.08.002.

Gapais, D., and B. Barbarin (1986), Quartz fabric transition in a cooling syntectonic granite (hermitage massif, france), Tectonophysics, 125(4), 357-370, doi: 10.1016/0040-1951(86)90171-X.

Gaudemer, Y., P. Tapponnier, and D. Turcotte (1989), River offsets across active strike-slip faults, Annales Tectonicae, 3(2), 55-76.

Ghent, E., and M. Stout (1984), TiO_2 activity in metamorphosed pelitic and basic rocks: principles and applications to metamorphism in southeastern canadian cordillera, Contribution to Mineral Petrology, 86(3), 248-255, doi: 10.1007/BF00373670.

Gilley, L., T. Harrison, P. Leloup, F. Ryerson, O. Lovera, and J.-H. Wang (2003), direct dating of left-lateral deformation along the red river shear zone, china and vietnam, Journal of Geophysical Research, 108(B2), 1-21, doi: 10.1029/2001JB001726.

Gleason, G., and J. Tullis (1995), A flow law for dislocation creep of quartz aggregates determined with the molten salt cell, Tectonophysics, 247(1-4), 1-23, doi: 10.1016/0040-1951(95)00011-B.

Grujic, D., M. Stipp, and J. L. Wooden (2011), Thermometry of quartz mylonites: Importance of dynamic recrystallization on Ti-in-quartz reequilibration, Geochemistry Geophysics Geosystems, 12(6), doi: 10.1029/2010GC003368.

Gueydan, F., C. Mehl, and T. Parra (2005), Stress- strain rate history of a midcrustal shear zone and the onset of brittle deformation inferred from quartz recristallized grain size, in: D Gapais, J.P. Brun and P.R. Cobbold (Editors), Deformation mechanisms, Rheology and Tectonics : from minerals to the lithosphere. Geological society of London., Special publications, 243, 127-142, doi: 10.1144/GSL.SP.2005.243.01.10.

Hammer, O., D. A. T. Harper, and P. D. Ryan (2001), Past: Paleontological statistics software package for education and data analysis., Paleontologia Electronica, 4(1), 9.

Handy, M. R. (1990), The solid-state flow of polymineralic rocks, Journal of Geophysical Research, 95(B6), 8647-8661, doi: 10.1029/JB095iB06p08647.

Harrison, T. M., C. Wenji, P. H. Leloup, F. J. Ryerson, and P. Tapponnier (1992), An early miocene transition in deformation regime within the red river fault zone, Yunnan, and its significance for indo-asian tectonics, Journal of Geophysical Research, 97(B5), 7159-7182, doi: 10.1029/92JB00109.

Harrison, T. M., P. H. Leloup, F. J. Ryerson, P. Tapponnier, R. Lacassin, C. wenji, A. Yin, and T. Harrison (1996), Diachronous initiation of transtension along the ailao shan-red river shear zone, yunnan and vietnam, In: Yin A., T.M. Harrison (Eds), The Tectonic Evolution of Asia. Cambridge University Press, Cambridge, pp. 208-226.

Helmcke, D. (1985), The permo-triassic "paleotethys" in mainland southeast-asia and adjacent parts of china, International Journal of Earth sciences, 74(2), 215-228, doi: 10.1007/BF01824893.

Hirth, G., and J. Tullis (1991), Dislocation creep regimes in quartz aggregates, Journal of Structural Geology, 14(2), 145-159, doi: 10.1016/0191-8141(92)90053-Y.

Hirth, G., C. Teyssier, and W. Dunlap (2001), An evaluation of quartzite flow laws based on comparisons between experimentally and naturally deformed rocks, International Journal of Earth sciences, 90(1), 77-87, doi: 10.1007/s005310000152.

Holyoke, C. W., and A. K. Kronenberg (2010), Accurate differential stress measurement using the molten salt cell and solid salt assemblies in the griggs apparatus with applications to strength, piezometers and rheology, Tectonophysics, 494(1-2), 17-31, doi: 10.1016/j.tecto.2010.08.001.

Huang, Z., and A. Audedat (2012), The titanium-in-quartz (titaniQ) thermobarometer: A critical examination and recalibration, Geochimica et Cosmochimica Acta, 84, 75-89, doi: 10.1016/j.gca.2012.01.009.

Huang, Z., L. Wang, M. Xu, J. Liu, N. Mi, and S. Liu (2007), Shear wave splitting across the ailao shan-red river fault zone, SW china, Geophysical research letters, 34(20), L20,301, doi: 10.1029/2007GL031236.

Jain, A., and S. Singh (2008), Tectonics of the southern Asian plate margin along the karakoram shear zone: Constraints from field observations and U/Pb shrimp ages, Tectonophysics, 451(1-4), 186-205, doi: 10.1016/j.tecto.2007.11.048.

Jerabek, P., H. Stunitz, R. Heilbronner, O. Lexa, and K. Schulmann (2007), Microstructural-deformation record of an orogen-parallel extension in the vepor unit, west carpathians, J. Struct. Geol., 29, 1722-1743, doi:10.1016/j.jsg.2007.09.002.

Jolivet, L., O. Beyssac, B. Goffé, D. Avigad, C. Lepvrier, H. Maluski, and T. T. Thang (2001), Oligo miocene midcrustal subhorizontal shear zone in indochina, Tectonics, 20(1), 46-57. doi:10.1029/2000TC900021.

Kidder, S., J. P. Avouac, and Y. C. Chan (2013), Application of titanium-in-quartz thermobarometry to greenschist facies veins and recrystallized quartzites in the hsuehshan range, taiwan, Solid Earth, 4, 1-21, doi:10.5194/se-4-1-2013.

Kilian, R., R. Heilbronner, and H. Stunitz (2011a), Quartz grain size reduction in a granitoid rock and the transition from dislocation to diffusion creep, Journal of Structural Geology, 33, 1265-1284, doi:10.1016/j.jsg.2011.05.004.

Kilian R., R. Heilbronner, and H. Stunitz (2011b), Quartz microstructures and crystallographic preferred orientation: Which shear sense do they indicate?, Journal of Structural Geology, 33, 1446–1466.

Kohn, M., and C. Northrup (2009), Taking mylonites' temperatures, Geology, 37, 47-50, doi: 10.1130/G25081A.1.

Lacassin, R., P. H. Leloup, and P. Tapponnier (1993), Bounds on strain in large tertiary shear zones of se asia from boudinage restoration, Journal of Structural Geology, 15(6), 677-692, doi: 10.1016/0191-8141(93)90055-F.

Lacassin, R., et al. (2004), Large-scale geometry, offset and kinematic evolution of the karakorum fault, tibet, Earth and Planetary Science Letters, 219(3-4), 255-269, doi: 10.1016/S0012-821X(04)00006-8.

Leloup, P., P. Tapponnier, and R. Lacassin (2007), Discussion on the role of the red river shear zone, yunnan and vietnam, in the continental extrusion of SE Asia, Journal of the Geological Society, 164, 1253-1260, doi: 10.1144/0016-76492007-065.

Leloup, P. H., and J. R. Kienast (1993), High-temperature metamorphism in a major strike-slip shear zone: the ailao shan-red river, people's republic of china, Earth and Planetary Science Letters, 118(1-4), 213-234, doi: 10.1016/0012-821X(93)90169-A.

Leloup, P. H., R. Lacassin, P. Tapponnier, U. Schärer, Z. Dalai, L. Xiaohan, Z. Liangshang, J. Shaocheng, and T. P. Trong (1995), The ailao shan-red river shear zone (yunnan, china), tertiary transform boundary of indochina, Tectonophysics, 251(1-4), 3-84, doi: 10.1016/0040-1951(95)00070-4.

Leloup, P. H., Y. Ricard, J. Battaglia, and R. Lacassin (1999), Shear heating in continental strike-slip shear zones: numerical modeling and case studies., Geophysical Journal International, 136(1), 19-40, doi: 10.1046/j.1365-246X.1999.00683.x.

Leloup, P. H., N. Arnaud, R. Lacassin, J. Kienast, T. Harrison, P. Trinh, A. Replumaz, and P. Tapponnier (2001), New constraints on the structure, thermochronology and timing of the ailao shan - red river shear zone, SE asia., Journal of Geophysical Research, 106(B4), 6683-6732, doi: 10.1029/2000JB900322.

Leloup, P. H., E. Boutonnet, W. J. Davis, and K. Hattori (2011), Long-lasting intracontinental strike-slip faulting: new evidence from the karakorum shear zone in the himalayas, Terra Nova, 23(2), 92-99, doi: 10.1111/j.1365-3121.2011.00988.x.

Luan, F. C., and M. S. Paterson (1992), Preparation and deformation of synthetic aggregates of quartz, Journal of Geophysical Research, 97(B1), 301-320, doi: 10.1029/91JB01748.

Mainprice, D., J. L. Bouchez, P. Blumenfeld, and J. M. Tubia (1986), Dominant c-slip in naturally deformed quartz: implications for dramatic plastic softening at high temperature, Geology, 14, 819-822, doi: 10.1130/0091-7613(1986)14.

Mancktelow, N. S., and G. Pennacchioni (2010), Why calcite can be stronger than quartz, Journal of Geophysical Research, 115(B1), doi:10.1029/2009JB006526.

Matte, P., P. Tapponnier, N. Arnaud, L. Bourjot, J. Avouac, P. Vidal, Q. Liu, Y. Pan, and Y. Wang (1996), Tectonics of Western Tibet between the Tarim and the indus, Earth and Planetary Science Letters, 142(3-4), 311-330, doi: 10.1016/0012-821X(96)00086-6.

McCarthy, M., and R. Weinberg (2010), Structural complexity resulting from pervasive ductile deformation in the karakoram shear zone, ladakh, NW india, Tectonics, 29(3), doi:10.1029/2008TC002354.

Menegon, L., G. Pennacchioni, R. Heilbronner, and L. Pittarello (2008), Evolution of quartz microstructure and c-axis crystallographic preferred orientation within ductilely deformed granitoids (arolla unit, western alps), Journal of Structural Geology, 30, 1332-1347, doi:10.1016/j.jsg.2008.07.007.

Mukherjee S. (2012), Simple shear is not so simple! Kinematics and shear senses in Newtonian viscous simple shear zones, Geological Magazine, 149, 819-826.

Mukherjee S. (2013), Channel flow extrusion model to constrain dynamic viscosity and Prandtl number of the Higher Himalayan Shear Zone, International Journal of Earth Sciences, 102, 1811-1835.

Mukherjee S, Mulchrone K. A. (2013), Viscous dissipation pattern in incompressible Newtonian simple shear zones: an analytical model, International Journal of Earth Sciences, 102, 1165-1170.

Müller, W., D. Aerden, and A. N. Halliday (2000), Isotopic dating of strain fringe increments, duration and rates of deformation in shear zones, Science, 288, 2195-2198, doi: 10.1126/science.288.5474.2195.

Nam, T. N., M. Toriumi, and T. Itaya (1998), P-t-t paths and post-metamorphic exhumation of the day nui con voi shear zone in vietnam, Tectonophysics, 290(3-4), 299-318. doi: 10.1016/S0040-1951(98)00054-7.

Negrini M., H. Stünitz, A. Berger, L. Morales, and L. Menegon (2013), The effect of deformation on the titaniQ geothermobarometer an experimental study, submitted to Contributions to Mineralogy and Petrology.

Park, Y., S. H. Yoo, and J. H. Ree (2006), Weakening of deforming granitic rocks with layer development at middle crust, Journal of Structural Geology, 28, 919-928, doi: 10.1016/j.jsg.2006.02.005.

Passchier, C. W., and R. A. J. Trouw (20058), Microtectonics, Springer Berlin Heidelberg (Eds), 2nd edition, 366p, doi: 10.1007/978-3-662-08734-3.

Paterson, M. S., and F. C. Luan (1990), Quartz rheology under geological conditions, In: Knipe, R.J., Rutter, E.H., (Eds), Deformation Mechanisms, Rheology and Tectonics, Geological Society Special Publications, 54, 299-307.

Pennacchioni, G., L. Menegon, B. Leiss, F. Nestola, and G. Bromiley (2010), Development of crystallographic preferred orientation and microstructure during plastic deformation of natural coarse-grained quartz veins, Journal of Geophysical Research, 115(B12), doi: 10.1029/2010JB007674.

Peternell, M., P. Hasalova, C. Wilson, S. Piazolo, and K. Schulmann (2010), Evaluating quartz crystallographic preferred orientations and the role of deformation partitioning using EBSD and fabric analyser techniques, Journal of Structural Geology, 32(6), 803-817, doi: 10.1016/j.jsg.2010.05.007.

Phillips, R., and M. Searle (2007), Macrostructural and microstructural architecture of the karakoram fault: relationship between magmatism and strike-slip faulting, Tectonics, 26(TC3017). doi: 10.1029/2006TC001946.

Phillips, R., R. Parrish, and M. Searle (2004), Age constraints on ductile deformation and long-term slip rates along the karakoram fault zone, ladakh, Earth and Planetary Science Letters, 226(3-4), 305-319, doi: 10.1016/j.epsl.2004.07.037.

Ramsay JG (1980), Shear zone geometry: a review. Journal of Structural Geology, 2, 83-99.

Reichardt, H., R. Weinberg, U. Andersson, and M. Fanning (2010), Hybridization of granitic magmas in the source: The origin of the karakoram batholith, ladakh, NW india, Lithos, 116(3-4), 249-272, doi: 10.1016/j.lithos.2009.11.013.

Replumaz, A., R. Lacassin, P. Tapponnier, and P. H. Leloup (2001), Large river offsets and plio-quaternary dextral slip rate on the red river fault (yunnan, china), Journal of Geophysical Research, 106, 819-836, doi: 10.1029/2000JB900135.

Ricard, Y., and D. Bercovici (2009), A continuum theory of grain size evolution and damage, J. geophys. Res., 114(B01204), doi: 10.1029/2007JB005491.

Rolland, Y., G. Mahéo, A. Pêcher, and I. Villa (2009), Synkinematic emplacement of the pangong metamorphic and magmatic complex along the karakorum fault (N Ladakh), Journal of Asian Earth Sciences, 34(1), 10-25, doi: 10.1016/j.jseaes.2008.03.009.

Roy, P., A. K. Jain, and S. Singh (2010), Microstructures of mylonites along the karakoram shear zone, Tangste valley, Pangong mountains, Karakoram, Journal Geological Society of India, 75(5), 679-694, doi: 10.1007/s12594-010-0065-1.

Rozel, A., Y. Ricard, and D. Bercovici (2011), A thermodynamically self-consistent damage equation for grain size evolution during dynamic recrystallization, Geophysical Journal International, 184(2), 719-728, doi: 10.1111/j.1365-246X.2010.04875.x.

Rutter, E., D. Faulkner, K. Brodie, R. Phillips, and M. Searle (2007), Rock deformation processes in the karakoram fault zone, eastern karakoram, ladakh, NW india, Journal of Structural Geology, 29, 1315-1326, doi:10.1016/j.jsg.2007.05.001.

Rutter, E. H., and K. H. Brodie (2004), Experimental intracrystalline plastic flow in hot-pressed synthetic quartzite prepared from brazilian quartz crystals, Journal of Structural Geology, 26(2), 259-270, doi: 10.1016/S0191-8141(03)00096-8.

Sassier, C., P. Leloup, D. Rubatto, O. Galland, Y. Yue, and D. Lin (2009), Direct measurement of strain rates in ductile shear zones: A new method based on syntectonic dikes, Journal of Geophysical Research -Solid Earth, 114(B1), B01406, doi: 10.1029/2008JB005597.

Schärer, U., L.-S. Zhang, and P. Tapponnier (1994), Duration of strike-slip movements in large shear zones: the red river belt, china., Earth and Planetary Science Letter, 126(4), 379-397, doi: 10.1016/0012-821X(94)90119-8.

Searle, M. (2006), Role of the red river shear zone, yunnan and vietnam, in the continental extrusion of se Asia, Journal of the Geological Society, 163, 1025-1036, doi: 10.1144/0016-76492005-144.

Searle, M., and R. Phillips (2007), Relationships between right-lateral shear along the Karakoram fault and metamorphism, magmatism, exhumation and uplift: evidence from the K2 –gasherbrum -pangong ranges, north pakistan and Ladakh, Journal of the Geological Society, 164, 439-450, doi: 10.1144/0016-76492006-072.

Searle, M., R. Weinberg, W. Dunlap, R. Holdsworth, S. A., and J. Dewey (1998), Transpressional tectonics along the karakoram fault zone, northern Ladakh: constraints on tibetan extrusion, In: Continental Transpressional and Transtensional Tectonics, Geological Society, London, Special Publications, 135, 307-326, doi: 10.1144/GSL.SP.1998.135.01.23.

Shimizu, I. (2008), Theories and applicability of grain size piezometers, the role of dynamic recrystallization mechanisms, Journal of Structural Geology, 30, 899-917, doi:10.1016/j.jsg.2008.03.004.

Slotemaker, A., and J. D. Bresser (2006), On the role of grain topology in dynamic grain growth – 2D microstructural modeling, Tectonophysics, 427(1-4), 73-93, doi: 10.1016/j.tecto.2006.05.017.

Spear, F., and D. Wark (2009), Cathodoluminescence imaging and titanium thermometry in metamorphic quartz, Journal of metamorphic geology, 27(3), 187-205, doi: 10.1111/j.1525-1314.2009.00813.x.

Stipp, M., and K. Kunze (2008), Dynamic recrystallization near the brittle-plastic transition in naturally and experimentally deformed quartz aggregates, Tectonophysics, 448(1-4), 77-97, doi: 10.1016/j.tecto.2007.11.041.

Stipp, M., and J. Tullis (2003), The recrystallized grain size piezometer for quartz, Geophysical Research Letters, 30(21), 2088-, doi:10.1029/2003GL018444.

Stipp, M., H. Stünitz, R. Heilbronner, and S. M. Schmid (2002a), Dynamic recrystallization of quartz, correlation between natural and experimental conditions, 170-190 pp., De Meer, D.,Drury, M.R., De Bresser, J.H.P., Pennock, G.M. (Eds.).

Stipp, M., H. Stünitz, R. Heilbronner, and S. M. Schmid (2002b), The eastern tonale fault zone: a `natural laboratory' for crystal plastic deformation of quartz over a temperature range from 250 to 700°C, Journal of Structural Geology, 24(12), 1861-1884, doi: 10.1016/S0191-8141(02)00035-4.

Stipp, M., J. Tullis, M. Scherwath, and J. Behrmann (2010), A new perspective on paleopiezometry: Dynamically recrystallized grain size distributions indicate mechanism changes, Geology, 38(8), 759-762, doi:10.1130/G31162.1.

Streule, M., Phillips, M. Searle, D. Waters, and M. Horstwood (2009), Evolution and chronology of the pangong metamorphic complex adjacent to the karakoram fault, ladakh: constraints from thermobarometry, metamorphic modelling and U/Pb geochronology, Journal of the Geological Society, 166, 919-932, doi: 10.1144/0016-76492008-117.

Tapponnier, P., and P. Molnar (1977), Active faulting and tectonics of china, Journal of Geophysical Research, 82(20), 2905-2930, doi: 10.1029/JB082i020p02905.

Tapponnier, P., G. Peltzer, R. Armijo, M. Coward, and A. Ries (1986), On the mechanics of the collision between India and Asia, In: Collision Tectonics, Coward M. and Ries A.C. (Eds), Geological Society Special Publications, 19, 115-157.

Tapponnier, P., R. L. P. H. Leloup, U. Scharer, Z. Dalai, W. Haiwei, L. Xiaohan, J. Shaocheng, Z. Lianshang, and Z. Jiayou (1990), The ailao shan/red river metamorphic belt: Tertiary left-lateral shear between indochina and south china, Nature, 343, 431-437, doi: 10.1038/343431a0.

Tapponnier, P., X. Zhiqin, F. Roger, B. Meyer, N. Arnaud, G. wittlinger, and Y. Jingsui (2001), Oblique stepwise rise and growth of the tibet plateau, Science, 294, 1671-1677, doi: 10.1126/science.105978.

Thomas, J., E. B. Watson, F. Spear, P. Shemella, S. Nayak, and A. Lanzirotti (2010), Titaniq under pressure, the effect of pressure and temperature on the solubility of Ti in quartz, Contributions to Mineralogy and Petrology, 160, 743-759, doi:10.1007/s00410-010-0505-3.

Tödheide, K. (1972), Water at High Temperatures and Pressure, In: Water, a Comprehensive Treatise, Franks F. (Ed), 1, 463-514, Plenum Press, New York.

Twiss, R. (1977), Theory and applicability of a recrystallized grain size paleopiezometer, Pure and Applied Geophysics, 115(1-2), 227-244, doi: 10.1007/BF01637105.

Valli, F., et al. (2007), 20 million years of continuous deformation along the karakorum fault, western tibet: a thermochronological analysis, Tectonics, 26(4), TC4004, doi: 10.1029/2005TC001913.

Wang, P. L., C. H. Lo, T. Y. Lee, S. L. Chung, C. Y. Lan, and N. T. Yem (1998), Thermochronological evidence for the movement of the ailao shan-red river shear zone: a perspective from vietnam, Geology, 26, 887-890, doi: 10.1130/0091-7613(1998)026.

Wark, D., and E. Watson (2006), Titaniq: a titanium-in-quartz geothermometer, Contribution to Mineral Petrology, 152, 743-754, doi:10.1007/s00410-006-0132-1.

Weinberg, R., W. Dunlap, M. Whitehouse, M. Khan, M. Searle, and M. Jan (2000), New field, structural and geochronological data from the Shyok and Nubra valleys, northern Ladakh: Linking Kohistan to Tibet, In: Tectonics of the Nanga Parbat Syntaxis and the Western Himalaya, Khan A., Treloar P.J., Searle, M.P. (Eds.), Geological Society of London, Special Publications, 170, 253-275.

Wright, T., B. Parsons, P. England, and E. Fielding (2004), Insar observations of low slip rates on the major faults of western tibet, Science, 305, 236-239, doi: 10.1126/science.1096388

Zhang, L.-S., and U. Schärer (1999), Age and origin of magmatism along the cenozoic red river shear belt, china, Contributions to Mineralogy and Petrology, 134(1), 67-85, doi: 10.1007/s004100050469.

TABLE 1. TITANIUM-IN-QUARTZ MEASUREMENTS

sample	^{47}Ti[b] (ppm)	^{48}Ti[b] (ppm)	^{49}Ti[b] (ppm)	Ti (ppm)[a] (ppm)	error (ppm)	TitaniQ Thermo-barometer[c] a	error	b	error
ASRR									
YU29	27.4 ±2.0		24.4 ±2.1	**25.9**	2.1	4.9E-02	1.2E-03	-35.01	2.22
YU42	10.5 ±1.7	10.2 ±2.6	9.5 ±2.1	**10.1**	2.1	5.4E-02	1.3E-03	-35.01	2.22
YU44	6.3 ±0.5		5.1 ±0.3	**5.7**	0.9	5.6E-02	4.2E-04	-35.01	2.22
YU61	64.5 ±8.3	63.5 ±7.3	64.2 ±7.7	**64.1**	8.3	4.5E-02	4.5E-03	-35.01	2.22
YU73 -ribbon	4.8 ±0.7	4.0 ±0.4	4.7 ±0.5	**4.5**	0.9	5.8E-02	4.8E-04	-35.01	2.22
YU73 -matrix	12.1 ±1.9	12.1 ±3.7	13.2 ±3.0	**12.5**	3.7				
YY33	15.0 ±0.7		14.1 ±0.9	**14.6**	1.8	5.2E-02	1.1E-03	-35.01	2.22
YY35	14.7 ±0.4		13.7 ±0.5	**14.3**	1.5	5.2E-02	3.6E-04	-35.01	2.22
YY54	61.9 ±1.1	61.5 ±1.3	61.6 ±2.9	**61.7**	2.9	4.5E-02	1.1E-03	-35.01	2.22
YY72	40.8 ±4.0	40.8 ±3.1	40.7 ±3.8	**40.8**	4.0	4.7E-02	2.1E-03	-35.01	2.22
KSZ									
LA26	6.4 ±0.4	5.9 ±0.4	6.5 ±0.5	**6.3**	0.4	5.6E-2	4.3E-4	-35.01	2.22
LA30	4.6 ±0.4	4.0 ±0.5	4.6 ±0.7	**4.8**	0.5	5.7E-2	4.6E-4	-35.01	2.22
LA42	1.9 ±0.4	1.4 ±0.2	1.9 ±0.3	**1.7**	0.3	6.2E-2	4.2E-4	-35.01	2.22
LA47	4.4 ±0.5	3.9 ±0.7	4.5 ±0.3	**4.3**	0.5	5.8E-2	4.5E-4	-35.01	2.22
LA59	4.6 ±0.7	3.6 ±0.6	4.6 ±0.8	**4.3**	0.7	5.8E-2	5.6E-4	-35.01	2.22

[a]: Ti contents are calculated by combining ^{47}Ti, ^{48}Ti (when available) and ^{49}Ti measurements.

[b]: Ti (ppm) calculated with the indicated Ti isotope

[c]: thermo-barometer calibrated by Thomas et al. [2010]: $P = a\,T + b$

TABLE 2. QSR STRAIN RATE MEASUREMENTS IN THE ASRR AND KFZ STRIKE-SLIP SHEAR ZONES

Shear zone/ sample	**Lat/Long**	Quartz vein size	Recrystalliza - tion regime[a]	Mean grain size measured (microns)	Mean grain size corrected[b] (microns)	Stress* (MPa)	Stress** (MPa)	Method of Temperature determination	Temperature (°C)	Pressure (MPa)	Hydrostatic pressure (MPa)		Strain rate[§] (s^{-1})	Strain rate[§§] (s^{-1})
<u>ASRR</u>														
YU29	23.767°N	mm	SGR	52.7	67.1	37.3	21.1	Ti-in-Quartz +	469	150	50		**1.9E-13**	**2.6E-13**
error (1 s)	101.710°E			±6.8	±10.2	±9.4	±9.6	P-T path	±44	±80	±25	max	1.6E-12	2.9E-12
												min	1.5E-14	9.9E-15
YU42	23.530° N	mm	SGR	92.9	118.3	27.8	13.4	Ti-in-Quartz +	402	120	32		**4.2E-15**	**7.3E-15**
error (1 s)	101.910°E			±6.8	±10.2	±5.3	±6.0	P-T path	±40	±80	±20	max	3.0E-14	8.1E-14
												min	4.3E-16	2.8E-16
YU44	23.530°N	cm	SGR	72.2	91.9	37.5	16.4	Ti-in-Quartz +	367	110	22		**2.5E-15**	**3.6E-15**
error (1 s)	101.910°E			±6.8	±10.2	±7.2	±7.3	P-T path	±40	±80	±15	max	1.5E-14	3.3E-14
												min	3.4E-16	1.8E-16
YU61	23.244°N	mm	SGR	61.9	78.9	28.1	18.5	Ti-in-Quartz +	548	180	80		**8.1E-13**	**1.4E-12**
error (1 s)	102.781°E			±6.8	±10.2	±7.5	±8.3	P-T path	±96	±70	±35	max	1.7E-11	3.6E-11
												min	1.7E-14	1.6E-14
YU73	23.530°N	cm	SGR	78.2	99.6	36.7	15.4	Ti-in-Quartz +	352	100	18		**1.1E-15**	**1.6E-15**
error (1 s)	101.910°E			±6.8	±10.2	±6.6	±6.8	P-T path	±40	±80	±13	max	6.1E-15	1.5E-14
												min	1.4E-16	8.0E-17
YY33	23.554°N	mm	SGR	63.3	80.6	35.6	18.2	Ti-in-Quartz +	425	130	34		**2.7E-14**	**4.2E-14**
error (1 s)	101.916°E			±6.8	±10.2	±7.9	±8.1	P-T path	±40	±80	±25	max	2.1E-13	4.6E-13
												min	2.4E-15	1.6E-15
YY35	23.554°N	cm	SGR	55.9	71.2	39.4	20.1	Ti-in-Quartz +	425	130	34		**4.0E-14**	**5.6E-14**
error (1 s)	101.916°E			±6.8	±10.2	±9.1	±9.1		±38	±80	±25	max	3.0E-13	5.9E-13
												min	3.7E-15	2.3E-15
YY54	24.277°N	cm	SGR	61.6	78.4	28.4	18.6	Ti-in-Quartz +	544	180	79		**7.6E-13**	**1.3E-12**
error (1 s)	101.378°E			±6.8	±10.2	±7.6	±8.3	P-T path	±51	±80	±32	max	6.3E-12	1.3E-11
												min	5.9E-14	5.6E-14
YY72	24.432°N	cm	SGR	36.0	45.8	46.8	28.5	Ti-in-Quartz +	507	160	72		**2.0E-12**	**1.9E-12**
error (1 s)	101.254°E			±6.8	±10.2	±14.6	±13.7	P-T path	±59	±80	±31	max	2.5E-11	2.8E-11
												min	8.2E-14	4.5E-14
<u>KSZ / PMC</u>														
LA26	34.025°N	cm	SGR	55.1	70.2	40.8	20.3	Ti-in-Quartz +	415	350	80		**8.0E-14**	**4.2E-14**
error (1 s)	78.171°E			±6.8	±10.2	±9.4	±9.2	P-T path	±40	±80	±37	max	4.5E-13	3.3E-13
												min	1.1E-14	2.5E-15
LA30	34.023°N	mm	SGR	39.2	49.9	55.7	26.6	Ti-in-Quartz +	400	350	80		**1.6E-13**	**5.6E-14**
error (1 s)	78.175°E			±6.8	±10.2	±14.8	±12.6	P-T path	±40	±80	±37	max	1.0E-12	4.6E-13
												min	1.8E-14	2.9E-15
LA52	34.039°N	mm	N.D.	-	-	-	-	-	-	-	-		**< 1.0E-15**	**< 1.0E-15**

error (1 s)	78.216°E			-	-	-	-	-	-	-	-	max	-	-
												min	-	-
LA59	34.052°N	cm	SGR	95.2	121.2	27.9	13.2	Ti-in-Quartz +	393	350	80		**8.0E-15**	**5.0E-15**
error (1 s)	78.245°E			±6.8	±10.2	±5.2	±5.2	P-T path	±40	±80	±37	max	4.0E-14	4.0E-14
												min	1.3E-15	3.0E-16
LA47	34.009°N	mm	SGR	31.8	40.5	67.0	31.4	Ti-in-Quartz +	394	350	80		**2.7E-13**	**7.5E-14**
error (1 s)	78.303°E			±6.8	±10.2	±20.3	±15.6	P-T path	±40	±80	±37	max	1.9E-12	6.5E-13
												min	2.4E-14	3.4E-15
LA44 (PMC)	33.971°N	cm	SGR	107.2	136.5	28.7	12.0	Ti-in-Quartz	350[c]	350[c]	*80*		**1.7E-15**	**6.9E-16**
error (1 s)	78.376°E			±6.8	±10.2	±4.8	±5.3	P-T path	±50	±80	*±37*	max	2.1E-14	1.5E-14
												min	8.3E-17	1.1E-17
LA42 (PMC)	33.971°N	cm	SGR /GBM[c]	140.5	178.8	23.4	9.7	Ti-in-Quartz +	347	350	80		**6.3E-16**	**3.1E-16**
error (1 s)	78.376°E			±6.8	±10.2	±3.7	±4.4	P-T path	±40	±80	±37	max	2.8E-15	2.4E-15
												min	1.2E-16	1.8E-17

Note: ASRR= Ailao Shan Red River ; KFZ= Karakorum Fault Zone; Recrystallization regime: SGR= sub-grain rotation; BLG= bulging. ; N.D.: No dynamic Recrystallization

Uncertainty calculation takes into account: the experimental measurement errors (LA-ICP-MS, microthermometry, grain size, P-T path, EBSD, Fabric analyser), the errors of equations calibration when available (piezometer, flow law, thermo-barometer) and they are propagated to measure the strain rate.

[a] The recrystallization regime is determined by the shape of the considered grains following criteria of Stipp et al. (2002). [b] Stereographic correction

[c]Uncertainties in the strain rate value due to the absence of Titanium-in-quartz measurements or defined recrytallization regime

Stress calculated using: *Shimizu (2008) or **Stipp and Tullis (2003) piezometer

Strain rates calculated using: [§]Hirth et al. (2001)/ Shimizu (2008) or [§§]Paterson and Luan (1990)/ Stipp and Tullis (2003) combination

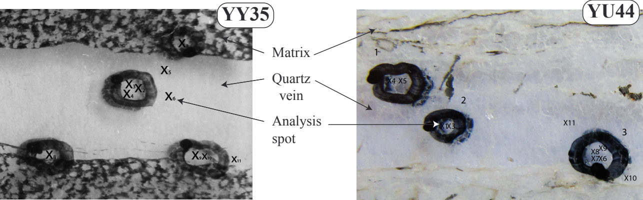
YY35
X5
X3X2
X4
X6
X8
X9X10
X11
Matrix
Quartz
vein
Analysis
spot
YU44
1
X4 X5
2
X1X3
X11
3
X8X9
X7X6
X10

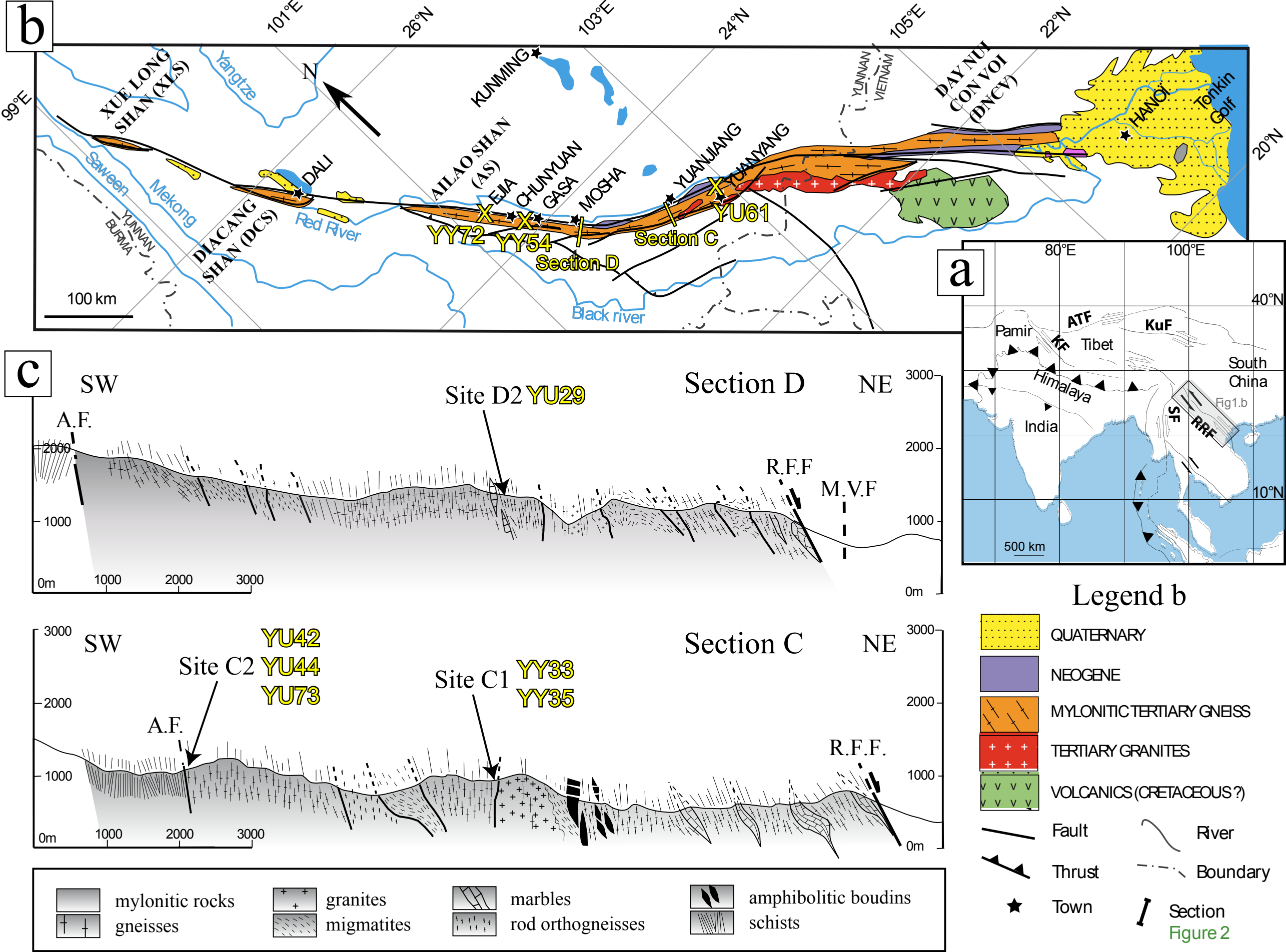
b
a
c
101°E
26°N
103°E
24°N
105°E
22°N
99°E
20°N
N
XUE LONG SHAN (XLS)
Yangtze
KUNMING
YUNNAN VIETNAM
DAY NUI CON VOI (DNCV)
HANOI
Tonkin Golf
Saween
Mekong
DALI
DIACANG SHAN (DCS)
Red River
AILAO SHAN (AS)
EJIA
CHUNYUAN
GASA
MOSHA
YUANJIANG
YUANYANG
YY72
YY54
Section D
Section C
YU61
YUNNAN BURMA
100 km
Black river
80°E
100°E
40°N
10°N
Pamir
ATF
KuF
KF
Tibet
South China
Himalaya
India
SF
RRF
Fig1.b
500 km
Legend b
QUATERNARY
NEOGENE
MYLONITIC TERTIARY GNEISS
TERTIARY GRANITES
VOLCANICS (CRETACEOUS ?)
Fault
River
Thrust
Boundary
Town
Section
Figure 2
SW
Section D
NE
Site D2 YU29
A.F.
R.F.F
M.V.F
3000
2000
1000
0m
SW
Section C
NE
YU42
Site C2 YU44
YU73
Site C1 YY33
YY35
A.F.
R.F.F.
mylonitic rocks
gneisses
granites
migmatites
marbles
rod orthogneisses
amphibolitic boudins
schists

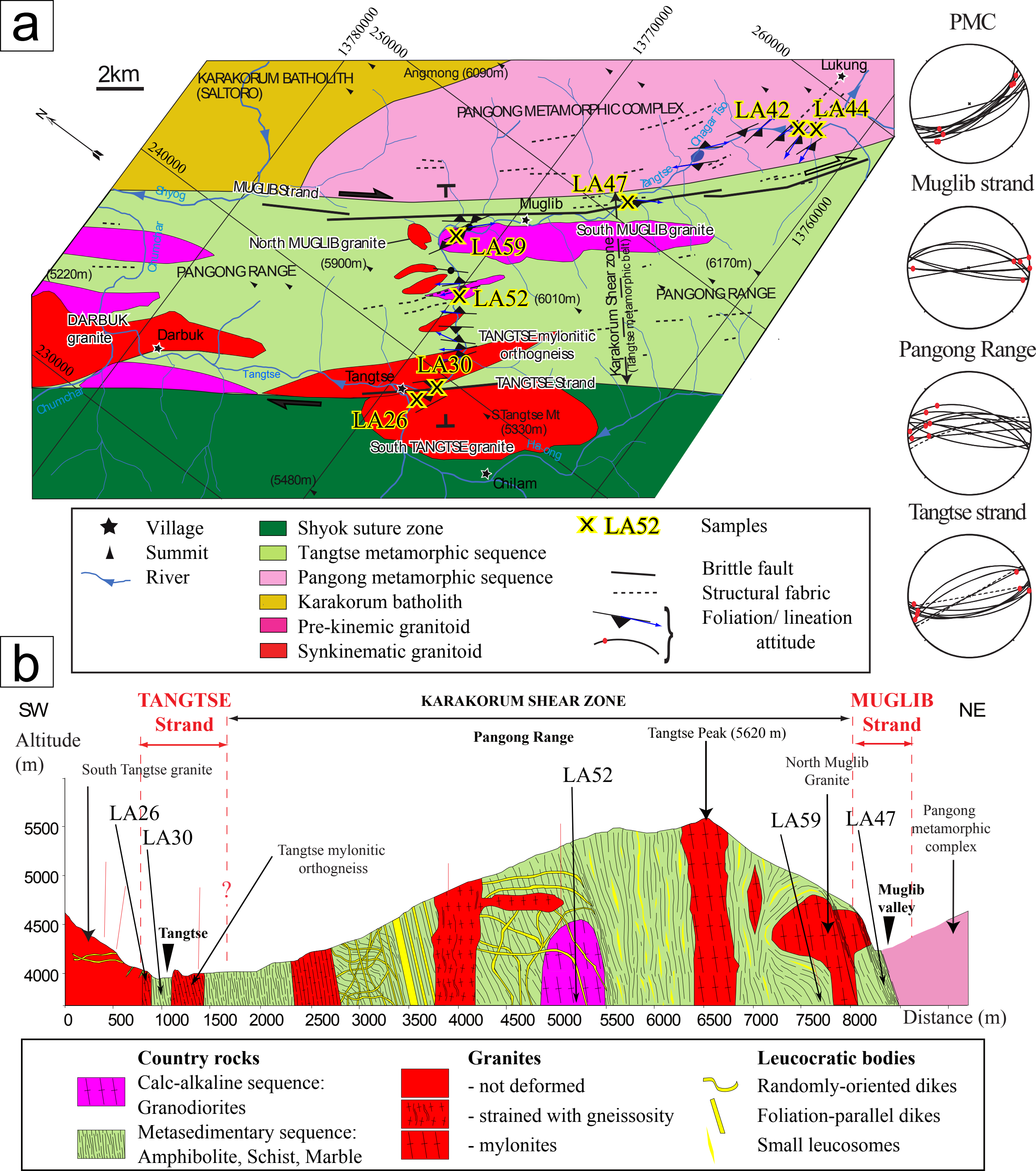
a
2km
KARAKORUM BATHOLITH (SALTORO)
Angmong (6090m)
PANGONG METAMORPHIC COMPLEX
Lukung
LA42
LA44
Chagar Tso
Tangtse
MUGLIB Strand
Shyog
Muglib
LA47
South MUGLIB granite
North MUGLIB granite
LA59
(5900m)
(6170m)
PANGONG RANGE
(5220m)
Chumchar
LA52
(6010m)
Karakorum Shear zone
(Tangtse metamorphic belt)
DARBUK granite
Darbuk
TANGTSE mylonitic orthogneiss
Tangtse
LA30
TANGTSE Strand
LA26
S Tangtse Mt (5330m)
South TANGTSE granite
Hanong
Chilam
(5480m)
13780000
250000
13770000
260000
13760000
240000
230000
Village
Summit
River
Shyok suture zone
Tangtse metamorphic sequence
Pangong metamorphic sequence
Karakorum batholith
Pre-kinemic granitoid
Synkinematic granitoid
LA52 Samples
Brittle fault
Structural fabric
Foliation/ lineation attitude
PMC
Muglib strand
Pangong Range
Tangtse strand
b
SW
NE
TANGTSE Strand
KARAKORUM SHEAR ZONE
MUGLIB Strand
Altitude (m)
Pangong Range
Tangtse Peak (5620 m)
South Tangtse granite
LA52
North Muglib Granite
LA26
LA30
LA59
LA47
Pangong metamorphic complex
Tangtse mylonitic orthogneiss
Tangtse
Muglib valley
5500
5000
4500
4000
0 500 1000 1500 2000 2500 3000 3500 4000 4500 5000 5500 6000 6500 7000 7500 8000
Distance (m)
Country rocks
Calc-alkaline sequence: Granodiorites
Metasedimentary sequence: Amphibolite, Schist, Marble
Granites
- not deformed
- strained with gneissosity
- mylonites
Leucocratic bodies
Randomly-oriented dikes
Foliation-parallel dikes
Small leucosomes

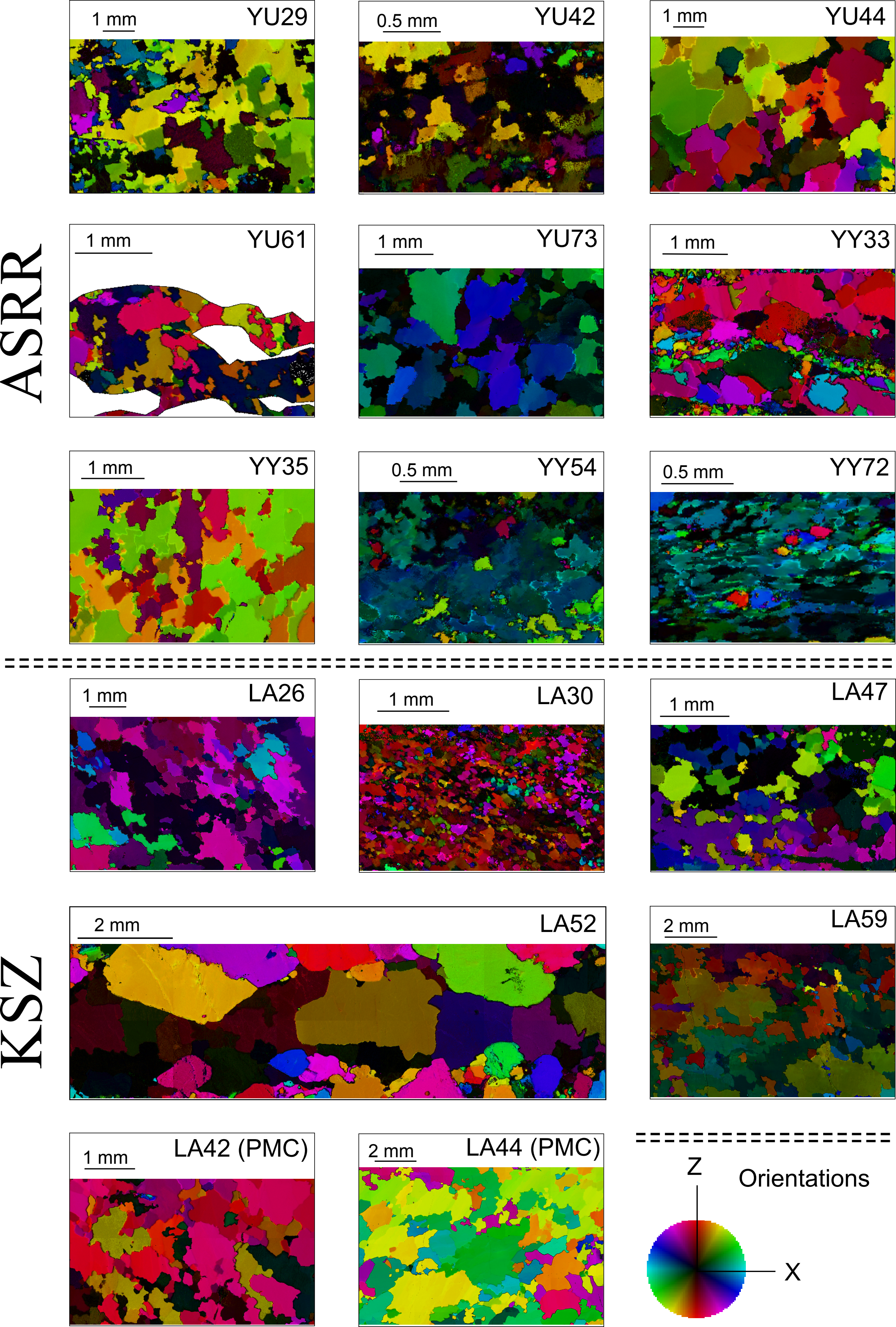

ASRR
1 mm
YU29
0.5 mm
YU42
1 mm
YU44
1 mm
YU61
1 mm
YU73
1 mm
YY33
1 mm
YY35
0.5 mm
YY54
0.5 mm
YY72
KSZ
1 mm
LA26
1 mm
LA30
1 mm
LA47
2 mm
LA52
2 mm
LA59
1 mm
LA42 (PMC)
2 mm
LA44 (PMC)
Z
Orientations
X

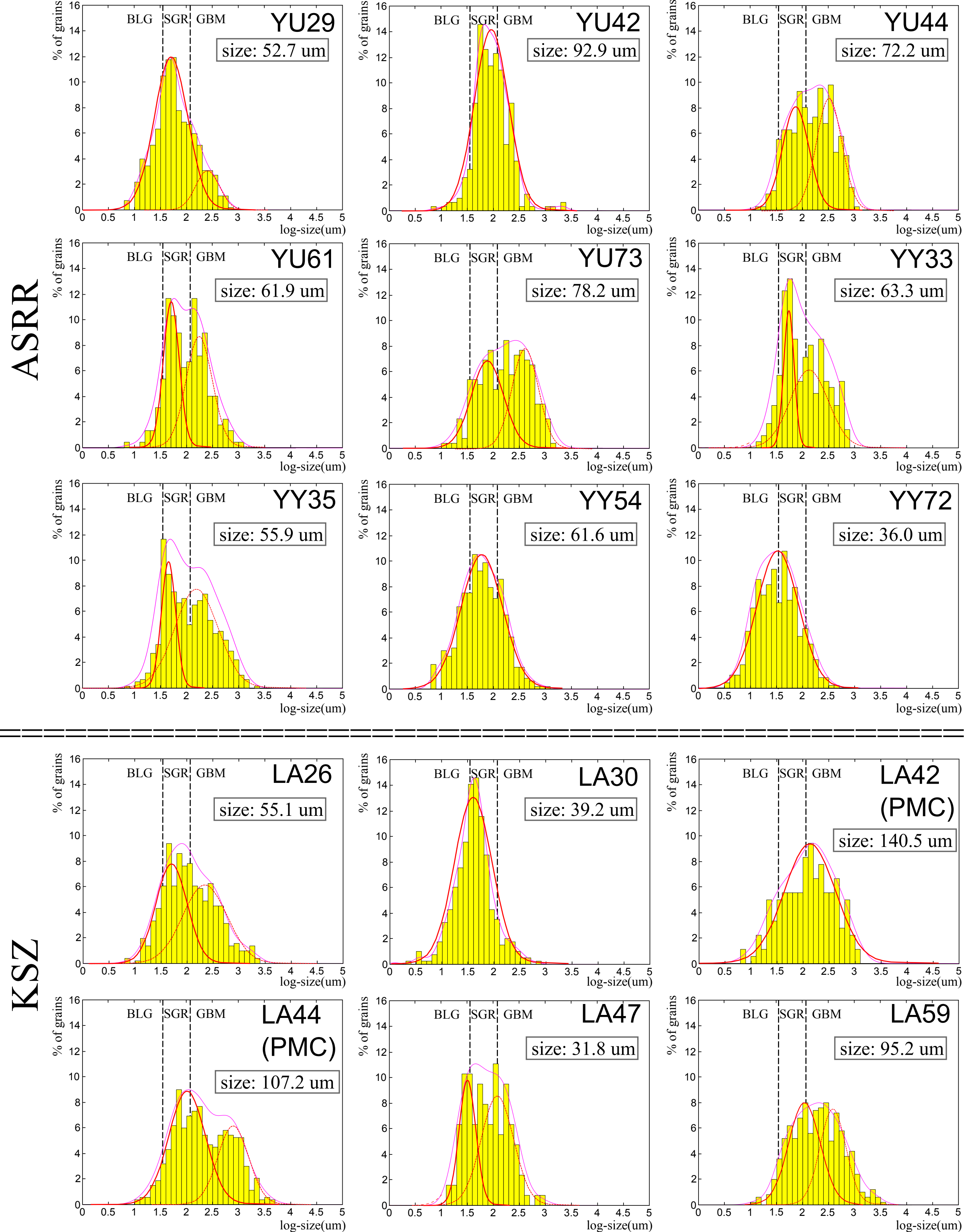
ASRR
KSZ
YU29
size: 52.7 um
YU42
size: 92.9 um
YU44
size: 72.2 um
YU61
size: 61.9 um
YU73
size: 78.2 um
YY33
size: 63.3 um
YY35
size: 55.9 um
YY54
size: 61.6 um
YY72
size: 36.0 um
LA26
size: 55.1 um
LA30
size: 39.2 um
LA42 (PMC)
size: 140.5 um
LA44 (PMC)
size: 107.2 um
LA47
size: 31.8 um
LA59
size: 95.2 um
BLG
SGR
GBM
% of grains
log-size(um)

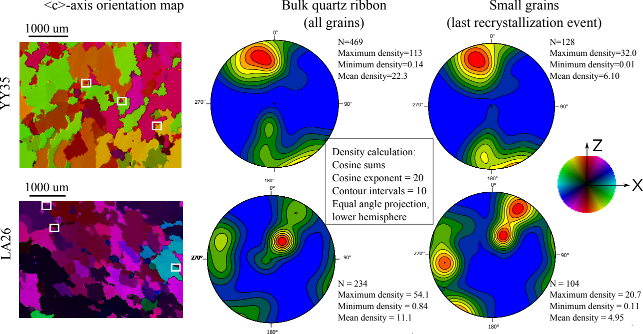

<c>-axis orientation map
Bulk quartz ribbon (all grains)
Small grains (last recrystallization event)
1000 um
YY35
N=469
Maximum density=113
Minimum density=0.14
Mean density=22.3
N=128
Maximum density=32.0
Minimum density=0.01
Mean density=6.10
Density calculation:
Cosine sums
Cosine exponent = 20
Contour intervals = 10
Equal angle projection, lower hemisphere
1000 um
LA26
N = 234
Maximum density = 54.1
Minimum density = 0.84
Mean density = 11.1
N = 104
Maximum density = 20.7
Minimum density = 0.11
Mean density = 4.95
Z
X
0°
90°
180°
270°

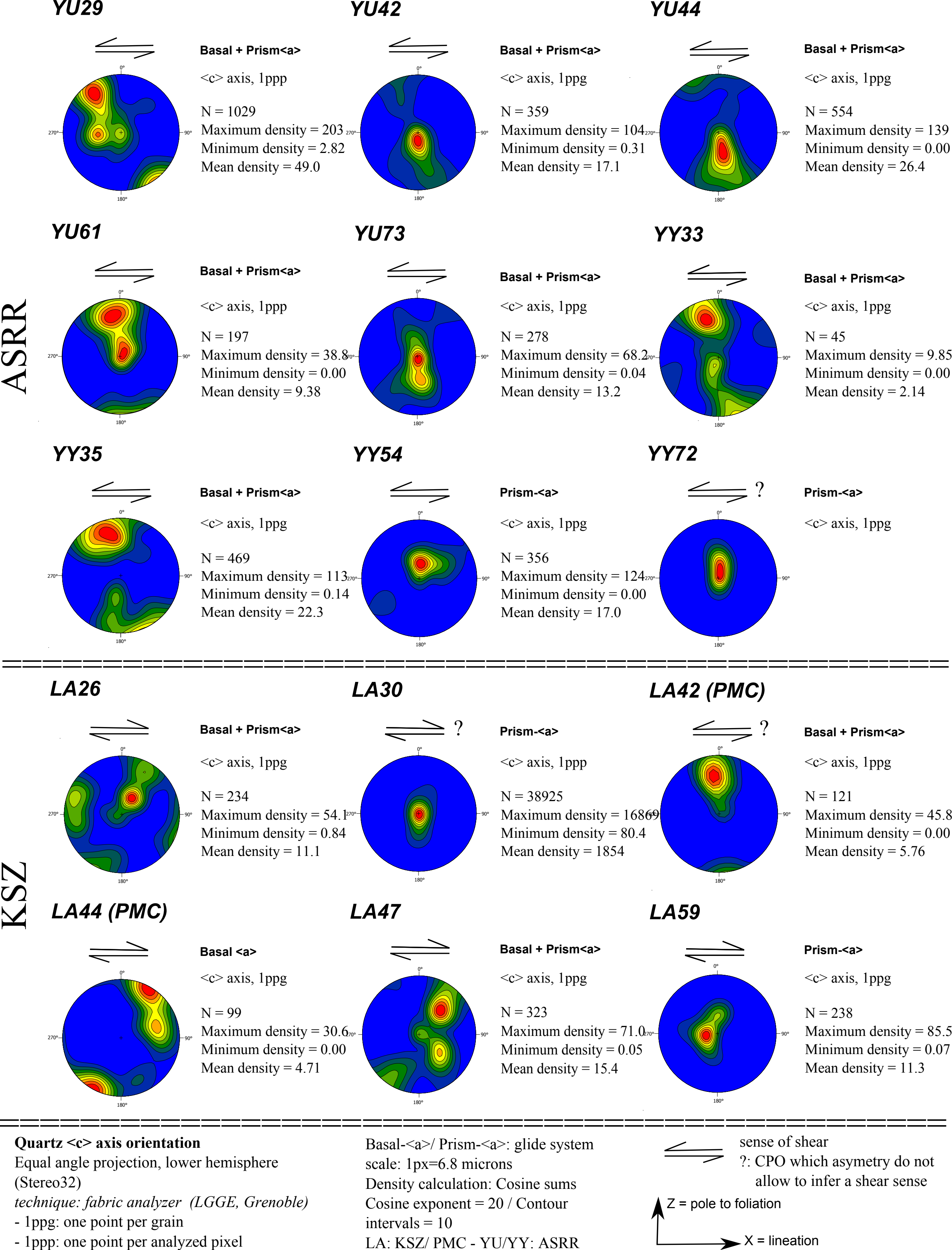
ASRR
YU29
Basal + Prism<a>
<c> axis, 1ppp
N = 1029
Maximum density = 203
Minimum density = 2.82
Mean density = 49.0
YU42
Basal + Prism<a>
<c> axis, 1ppg
N = 359
Maximum density = 104
Minimum density = 0.31
Mean density = 17.1
YU44
Basal + Prism<a>
<c> axis, 1ppg
N = 554
Maximum density = 139
Minimum density = 0.00
Mean density = 26.4
YU61
Basal + Prism<a>
<c> axis, 1ppp
N = 197
Maximum density = 38.8
Minimum density = 0.00
Mean density = 9.38
YU73
Basal + Prism<a>
<c> axis, 1ppg
N = 278
Maximum density = 68.2
Minimum density = 0.04
Mean density = 13.2
YY33
Basal + Prism<a>
<c> axis, 1ppg
N = 45
Maximum density = 9.85
Minimum density = 0.00
Mean density = 2.14
YY35
Basal + Prism<a>
<c> axis, 1ppg
N = 469
Maximum density = 113
Minimum density = 0.14
Mean density = 22.3
YY54
Prism-<a>
<c> axis, 1ppg
N = 356
Maximum density = 124
Minimum density = 0.00
Mean density = 17.0
YY72
?
Prism-<a>
<c> axis, 1ppg
KSZ
LA26
Basal + Prism<a>
<c> axis, 1ppg
N = 234
Maximum density = 54.1
Minimum density = 0.84
Mean density = 11.1
LA30
?
Prism-<a>
<c> axis, 1ppp
N = 38925
Maximum density = 16869
Minimum density = 80.4
Mean density = 1854
LA42 (PMC)
?
Basal + Prism<a>
<c> axis, 1ppg
N = 121
Maximum density = 45.8
Minimum density = 0.00
Mean density = 5.76
LA44 (PMC)
Basal <a>
<c> axis, 1ppg
N = 99
Maximum density = 30.6
Minimum density = 0.00
Mean density = 4.71
LA47
Basal + Prism<a>
<c> axis, 1ppg
N = 323
Maximum density = 71.0
Minimum density = 0.05
Mean density = 15.4
LA59
Prism-<a>
<c> axis, 1ppg
N = 238
Maximum density = 85.5
Minimum density = 0.07
Mean density = 11.3
0°
90°
180°
270°
Quartz <c> axis orientation
Equal angle projection, lower hemisphere (Stereo32)
technique: fabric analyzer (LGGE, Grenoble)
- 1ppg: one point per grain
- 1ppp: one point per analyzed pixel
Basal-<a>/ Prism-<a>: glide system
scale: 1px=6.8 microns
Density calculation: Cosine sums
Cosine exponent = 20 / Contour intervals = 10
LA: KSZ/ PMC - YU/YY: ASRR
sense of shear
?: CPO which asymetry do not allow to infer a shear sense
Z = pole to foliation
X = lineation

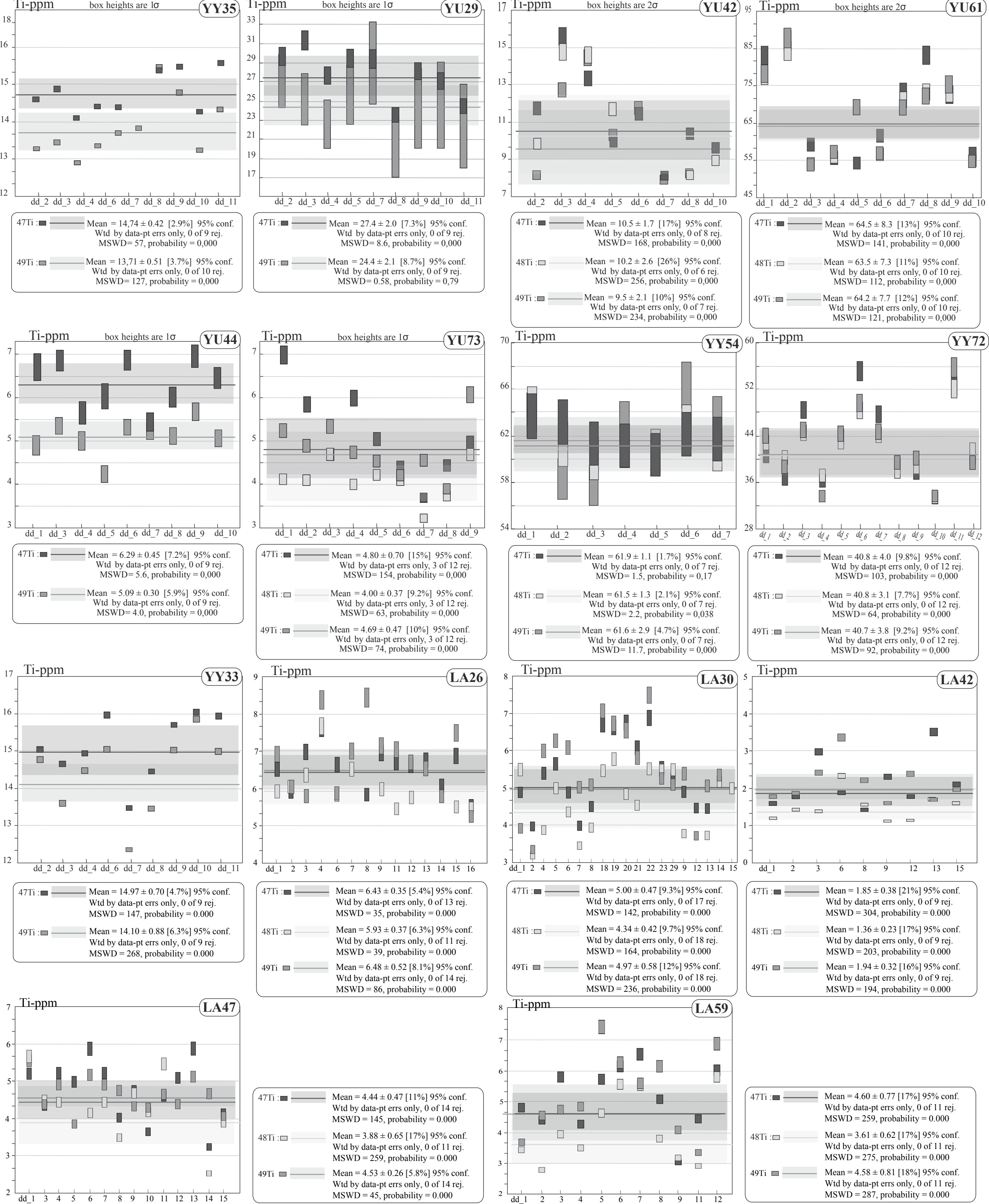

YY35
Ti-ppm
box heights are 1σ
47Ti : Mean = 14,74 ± 0.42 [2.9%] 95% conf. Wtd by data-pt errs only, 0 of 9 rej. MSWD= 57, probability = 0,000
49Ti : Mean = 13,71 ± 0.51 [3.7%] 95% conf. Wtd by data-pt errs only, 0 of 10 rej. MSWD= 127, probability = 0,000
YU29
Ti-ppm
box heights are 1σ
47Ti : Mean = 27.4 ± 2.0 [7.3%] 95% conf. Wtd by data-pt errs only, 0 of 9 rej. MSWD= 8.6, probability = 0,000
49Ti : Mean = 24.4 ± 2.1 [8.7%] 95% conf. Wtd by data-pt errs only, 0 of 9 rej. MSWD= 0.58, probability = 0,79
YU42
Ti-ppm
box heights are 2σ
47Ti : Mean = 10.5 ± 1.7 [17%] 95% conf. Wtd by data-pt errs only, 0 of 8 rej. MSWD= 168, probability = 0,000
48Ti : Mean = 10.2 ± 2.6 [26%] 95% conf. Wtd by data-pt errs only, 0 of 6 rej. MSWD= 256, probability = 0,000
49Ti : Mean = 9.5 ± 2.1 [10%] 95% conf. Wtd by data-pt errs only, 0 of 7 rej. MSWD= 234, probability = 0,000
YU61
Ti-ppm
box heights are 2σ
47Ti : Mean = 64.5 ± 8.3 [13%] 95% conf. Wtd by data-pt errs only, 0 of 10 rej. MSWD= 141, probability = 0,000
48Ti : Mean = 63.5 ± 7.3 [11%] 95% conf. Wtd by data-pt errs only, 0 of 10 rej. MSWD= 112, probability = 0,000
49Ti : Mean = 64.2 ± 7.7 [12%] 95% conf. Wtd by data-pt errs only, 0 of 10 rej. MSWD= 121, probability = 0,000
YU44
Ti-ppm
box heights are 1σ
47Ti : Mean = 6.29 ± 0.45 [7.2%] 95% conf. Wtd by data-pt errs only, 0 of 9 rej. MSWD= 5.6, probability = 0,000
49Ti : Mean = 5.09 ± 0.30 [5.9%] 95% conf. Wtd by data-pt errs only, 0 of 9 rej. MSWD= 4.0, probability = 0,000
YU73
Ti-ppm
box heights are 1σ
47Ti : Mean = 4.80 ± 0.70 [15%] 95% conf. Wtd by data-pt errs only, 3 of 12 rej. MSWD= 154, probability = 0,000
48Ti : Mean = 4.00 ± 0.37 [9.2%] 95% conf. Wtd by data-pt errs only, 3 of 12 rej. MSWD= 63, probability = 0,000
49Ti : Mean = 4.69 ± 0.47 [10%] 95% conf. Wtd by data-pt errs only, 3 of 12 rej. MSWD= 74, probability = 0,000
YY54
Ti-ppm
47Ti : Mean = 61.9 ± 1.1 [1.7%] 95% conf. Wtd by data-pt errs only, 0 of 7 rej. MSWD= 1.5, probability = 0,17
48Ti : Mean = 61.5 ± 1.3 [2.1%] 95% conf. Wtd by data-pt errs only, 0 of 7 rej. MSWD= 2.2, probability = 0,038
49Ti : Mean = 61.6 ± 2.9 [4.7%] 95% conf. Wtd by data-pt errs only, 0 of 7 rej. MSWD= 11.7, probability = 0,000
YY72
Ti-ppm
47Ti : Mean = 40.8 ± 4.0 [9.8%] 95% conf. Wtd by data-pt errs only, 0 of 12 rej. MSWD= 103, probability = 0,000
48Ti : Mean = 40.8 ± 3.1 [7.7%] 95% conf. Wtd by data-pt errs only, 0 of 12 rej. MSWD= 64, probability = 0,000
49Ti : Mean = 40.7 ± 3.8 [9.2%] 95% conf. Wtd by data-pt errs only, 0 of 12 rej. MSWD= 92, probability = 0,000
YY33
Ti-ppm
47Ti : Mean = 14.97 ± 0.70 [4.7%] 95% conf. Wtd by data-pt errs only, 0 of 9 rej. MSWD = 147, probability = 0.000
49Ti : Mean = 14.10 ± 0.88 [6.3%] 95% conf. Wtd by data-pt errs only, 0 of 9 rej. MSWD = 268, probability = 0.000
LA26
Ti-ppm
47Ti : Mean = 6.43 ± 0.35 [5.4%] 95% conf. Wtd by data-pt errs only, 0 of 13 rej. MSWD = 35, probability = 0.000
48Ti : Mean = 5.93 ± 0.37 [6.3%] 95% conf. Wtd by data-pt errs only, 0 of 11 rej. MSWD = 39, probability = 0.000
49Ti : Mean = 6.48 ± 0.52 [8.1%] 95% conf. Wtd by data-pt errs only, 0 of 14 rej. MSWD = 86, probability = 0.000
LA30
Ti-ppm
47Ti : Mean = 5.00 ± 0.47 [9.3%] 95% conf. Wtd by data-pt errs only, 0 of 17 rej. MSWD = 142, probability = 0.000
48Ti : Mean = 4.34 ± 0.42 [9.7%] 95% conf. Wtd by data-pt errs only, 0 of 18 rej. MSWD = 164, probability = 0.000
49Ti : Mean = 4.97 ± 0.58 [12%] 95% conf. Wtd by data-pt errs only, 0 of 18 rej. MSWD = 236, probability = 0.000
LA42
Ti-ppm
47Ti : Mean = 1.85 ± 0.38 [21%] 95% conf. Wtd by data-pt errs only, 0 of 9 rej. MSWD = 304, probability = 0.000
48Ti : Mean = 1.36 ± 0.23 [17%] 95% conf. Wtd by data-pt errs only, 0 of 9 rej. MSWD = 203, probability = 0.000
49Ti : Mean = 1.94 ± 0.32 [16%] 95% conf. Wtd by data-pt errs only, 0 of 9 rej. MSWD = 194, probability = 0.000
LA47
Ti-ppm
47Ti : Mean = 4.44 ± 0.47 [11%] 95% conf. Wtd by data-pt errs only, 0 of 14 rej. MSWD = 145, probability = 0.000
48Ti : Mean = 3.88 ± 0.65 [17%] 95% conf. Wtd by data-pt errs only, 0 of 11 rej. MSWD = 259, probability = 0.000
49Ti : Mean = 4.53 ± 0.26 [5.8%] 95% conf. Wtd by data-pt errs only, 0 of 14 rej. MSWD = 45, probability = 0.000
LA59
Ti-ppm
47Ti : Mean = 4.60 ± 0.77 [17%] 95% conf. Wtd by data-pt errs only, 0 of 11 rej. MSWD = 259, probability = 0.000
48Ti : Mean = 3.61 ± 0.62 [17%] 95% conf. Wtd by data-pt errs only, 0 of 11 rej. MSWD = 275, probability = 0.000
49Ti : Mean = 4.58 ± 0.81 [18%] 95% conf. Wtd by data-pt errs only, 0 of 11 rej. MSWD = 287, probability = 0.000

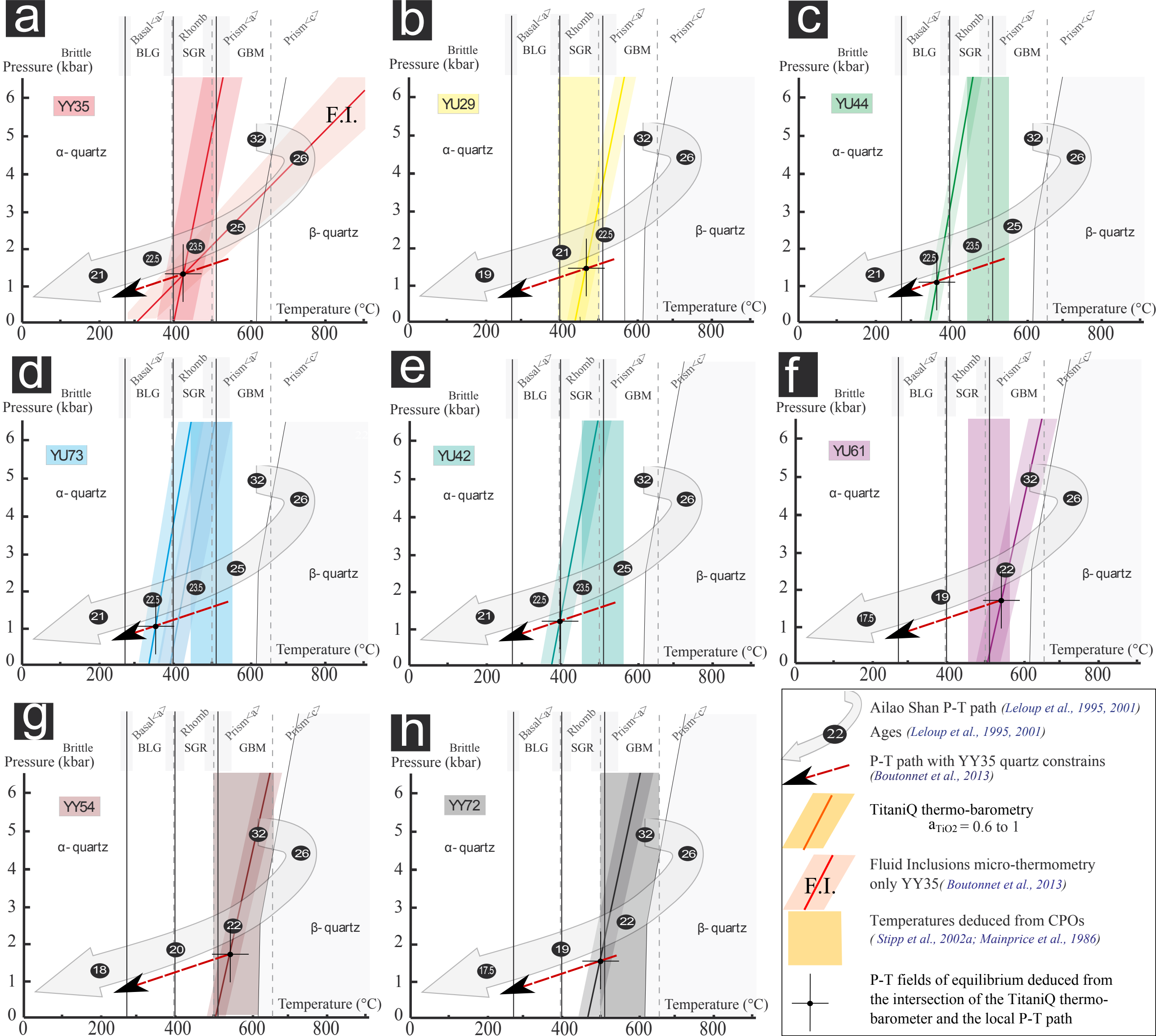
a
YY35
F.I.
b
YU29
c
YU44
d
YU73
e
YU42
f
YU61
g
YY54
h
YY72
Brittle
BLG
SGR
GBM
Basal<a>
Rhomb
Prism<a>
Prism<c>
Pressure (kbar)
Temperature (°C)
α- quartz
β- quartz
Ailao Shan P-T path (Leloup et al., 1995, 2001)
Ages (Leloup et al., 1995, 2001)
P-T path with YY35 quartz constrains (Boutonnet et al., 2013)
TitaniQ thermo-barometry a_{TiO2} = 0.6 to 1
Fluid Inclusions micro-thermometry only YY35 (Boutonnet et al., 2013)
Temperatures deduced from CPOs (Stipp et al., 2002a; Mainprice et al., 1986)
P-T fields of equilibrium deduced from the intersection of the TitaniQ thermo-barometer and the local P-T path

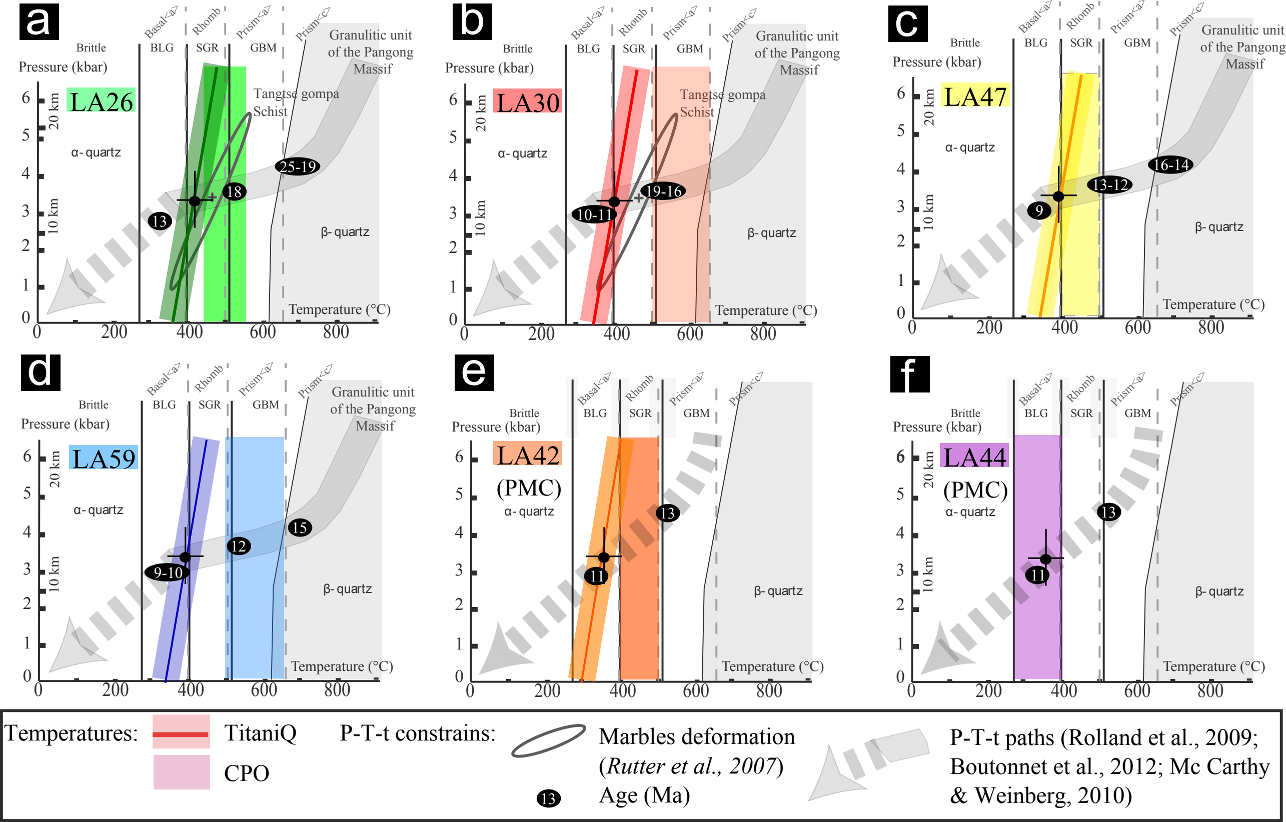

a
b
c
d
e
f
LA26
LA30
LA47
LA59
LA42
(PMC)
LA44
(PMC)
Pressure (kbar)
Temperature (°C)
Brittle
BLG
SGR
GBM
Basal<a>
Rhomb
Prism<a>
Prism<c>
Granulitic unit of the Pangong Massif
Tangtse gompa Schist
α- quartz
β- quartz
20 km
10 km
25-19
18
13
19-16
10-11
16-14
13-12
9
15
12
9-10
11
Temperatures:
TitaniQ
CPO
P-T-t constrains:
Marbles deformation (Rutter et al., 2007)
Age (Ma)
P-T-t paths (Rolland et al., 2009; Boutonnet et al., 2012; Mc Carthy & Weinberg, 2010)

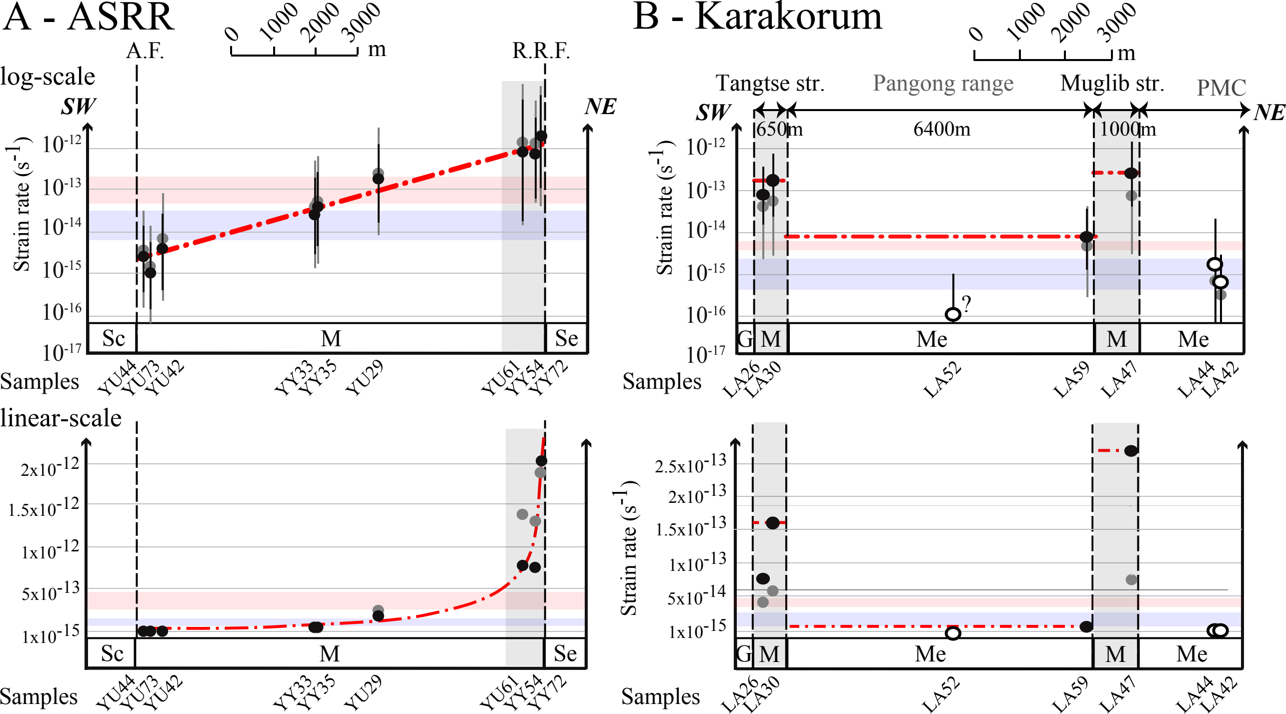

A - ASRR
B - Karakorum
log-scale
linear-scale
A.F.
R.R.F.
0 1000 2000 3000 m
SW
NE
Strain rate (s-1)
Sc
M
Se
Samples
YU44 YU73 YU42 YY33 YY35 YU29 YU61 YY54 YY72
Tangtse str.
Pangong range
Muglib str.
PMC
650m
6400m
1000m
G
Me
LA26 LA30 LA52 LA59 LA47 LA44 LA42
?

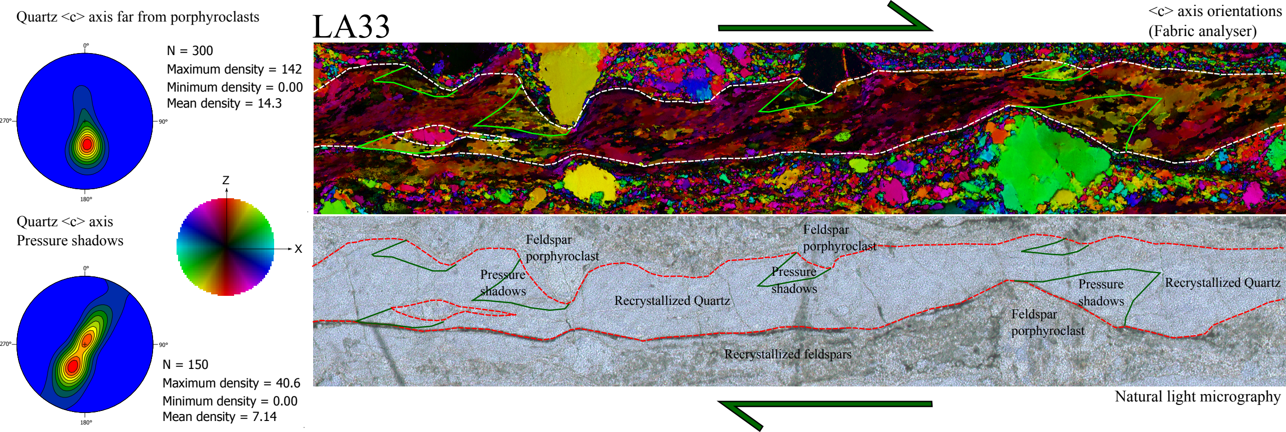
Quartz <c> axis far from porphyroclasts
0°
270°
90°
180°
N = 300
Maximum density = 142
Minimum density = 0.00
Mean density = 14.3
Quartz <c> axis
Pressure shadows
Z
X
0°
270°
90°
180°
N = 150
Maximum density = 40.6
Minimum density = 0.00
Mean density = 7.14
LA33
<c> axis orientations
(Fabric analyser)
Feldspar porphyroclast
Pressure shadows
Feldspar porphyroclast
Pressure shadows
Recrystallized Quartz
Pressure shadows
Recrystallized Quartz
Feldspar porphyroclast
Recrystallized feldspars
Natural light micrography